Vortex filament simulation of the turbulent coflowing jet

Peter S. Bernard[a)]
Department of Mechanical Engineering, University of Maryland, College Park, Maryland 20742, USA

(Received 6 October 2008; accepted 8 January 2009; published online 27 February 2009)

A high resolution grid-free vortex filament scheme is applied to the prediction and simulation of coflowing round jets with a view to acquiring a new perspective on their physics and establishing the validity of the numerical technique. Vortex loop removal at inertial range scales provides a nondiffusive model of local dissipation that remains compatible with the presence of backscatter. Consistency with the Kolmogorov −5/3 inertial range spectrum is used to estimate the effective dissipation rate and subsequently the local and global Reynolds numbers associated with the turbulent vortex field. New insights into the accuracy of the scheme are presented including dependencies on numerical parameters. Comparisons of the computed statistics and structural features of the coflowing jet versus experiments show the method to provide an accurate rendering of the flow. Some consideration is also given to the dispersion of a scalar contaminant in the jet and its comparison to data. © *2009 American Institute of Physics*. [DOI: 10.1063/1.3081559]

I. INTRODUCTION

Complex phenomena associated with turbulent jets, such as sound generation[1–3] and the dispersion of continuous or discrete contaminants,[4–6] are often tied to the presence of nonsteady turbulent vortical structures. Thus, the successful simulation of jet flows including complex physics requires numerical methodologies that offer a physically accurate representation of the continuously changing vortical aspects of the turbulent jet field. Under these circumstances, large eddy simulation (LES) represents a favored direction to take by virtue of its practicality and reduced role for modeling.

A number of grid-based LES formulations have been applied to the prediction of turbulent jet flows. Among these, Olsson and Fuchs[7] applied a dynamic model in studying the near field of a circular jet noting the effects of grid resolution, modeling parameters, and Reynolds number. Webb and Mansour[8] considered a forced round jet at relatively low Reynolds number using a dynamic model and found that the turbulence scales agreed with experiments. A simulation of compressible subsonic jets by Zhao *et al.*[9] with several variants of the dynamic model also included prediction of far field sound radiation. Borg *et al.*[10] used LES without an explicit subgrid model to simulate the entry region of a circular jet and included a concentration field so as to predict mass fluxes. Debonis and Scott[2] used a compressible form of the Smagorinsky model to simulate a high Reynolds number jet, with some success in matching the correct physics. The effectiveness of different subgrid models in computing compressible jet flows was examined by Bogey and Bailly[3,11] who noted the influence of the subgrid models in effectively lowering the Reynolds number.

As in numerous other flows where LES has been applied, many of the properties of jets observed in the aforementioned studies are sensitive to the particular form of the adopted subgrid models, as well as parameter choices and grid resolution. These effects are in part symptomatic of the persistent problem of crafting subgrid models that can accurately regulate the subtle physics governing local variations in the two-way flow of energy between the resolved and unresolved scales. Any oversimplification of the energy flux creates an opening for the appearance of numerical diffusion that can eliminate vortical flow features that are of central importance to the physics. For phenomena such as sound generation and particle dispersion that depend precisely on the vortices, a degree of uncertainty is injected into the numerical predictions and the accuracy can be compromised.

Vortex methods,[12] in which the computational elements are freely convecting vortices, have minimal exposure to numerical diffusion and thus, in principle, an increased likelihood of predicting the natural motion of vortical structures. Grid-free schemes relying on vortex filaments have been used in a number of prior jet studies that focused on the laminar and early transitional regimes. Among these, Chung and Troutt[4] considered particle dispersion in an axisymmetric jet in which the computational elements were vortex rings, while Agui and Hesselink[13] used a single layer of vortex rings with streamwise periodicity to model the evolution of the vortex transition including the appearance of streamwise vorticity. Similarly, Martin and Meiburg[14,15] used a vortex filament scheme with periodic boundary conditions to simulate the effect of perturbations on the vortical makeup of jets. In more recent times, Marzouk and Ghoniem[16] used a variant of the vortex filament method to study the vortex structure of a transitioning transverse jet including the initial breakdown of the flow into turbulence.

The adaptation of vortex methods to the direct numerical simulation (DNS) of turbulence in which all flow scales including small viscous dissipative eddies are resolved requires a formidable computational effort as well as a means for the accurate representation of viscous forces over a Lagrangian field of vortex elements. Some success in fulfilling the latter requirement in the context of a simulation of decaying isotropic turbulence has been achieved by periodically redistributing vortex particles.[17] Alternatively, a traditional mesh can be introduced to aid in vorticity redistribution and in the

[a)]Electronic mail: bernard@umd.edu.

evaluation of the viscous and stretching terms. Such hybrid schemes have been used to study isotropic turbulence[18] and in reproducing qualitative features of viscous vortex flows in free space.[19]

For turbulent flows of some complexity, such as the round jets of interest in this study, the most practical implementation of a vortex method is in the context of a LES and not a DNS. In this regard it has been proposed[20] to base a LES on the hybrid vortex particle method by appending a traditional diffusive subgrid model. However, in a LES the direct treatment of viscous forces acting below the threshold of resolved scales is not necessary so that alternatives to vortex particle methods, such as the vortex filament scheme used here, may be considered.

The success of a vortex method in simulating turbulent jets in the context of a LES depends primarily on how the fundamental representation of energy transfer to and from "subgrid" scales is handled. For a vortex filament scheme, in which the computational elements are short, straight, vortex tubes linked end to end forming filaments, it has been suggested[21,22] and previous work verified[23,24] that the excision of vortex loops naturally forming from highly stretched vortex filaments provides an elegant and effective means of accounting for the subgrid energy transfer process. In fact, removal of loops as they form provides local dissipation—since loops contribute primarily to the local velocity field—that would ordinarily be occurring at much smaller scales by the action of viscosity. At the same time, unlike diffusive subgrid models, loop removal does not inhibit local backscatter where vortices congregate forming larger scale structures. Computations have shown[23,24] that the use of loop removal is sufficient to limit growth in the number of vortex elements to practical limits and that the simulated turbulent field remains fully consistent with many fundamental properties of turbulence.

The present work considers the capabilities of the filament scheme in simulating coflowing turbulent round jets with an interest in providing a new perspective on their physics. For example, the vortex simulations prove useful in elucidating such aspects of the jet flow as the connection between coflow, the potential core, and vortical structures. In recognition of the relative novelty of the filament scheme as applied to turbulent flow, some attention is also directed at providing further understanding of the numerical properties of the filament scheme, such as the importance of numerical parameters, and in more precisely characterizing the Reynolds numbers associated with the turbulent field of vortices. Finally, calculations including passive tracer particles are performed that provide for additional comparisons with experiments and allow for a fresh look to be taken at differences between the development of the velocity and scalar fields.

II. THE VORTEX FILAMENT SCHEME

In the vortex filament scheme, straight vortex tubes strung end to end forming filaments are the principal computational element. The ith tube of N total is represented by its end points $\mathbf{x}_i^1$ and $\mathbf{x}_i^2$ and a circulation, say, Γ_i, that it shares in common with other tubes on the same filament. The circulation is assigned to each filament at its inception—usually at a boundary—and remains fixed for all time consistent with Kelvin's theorem and the relegation of viscous effects to small, invisible scales.

The time evolution of the flow is accounted for by convecting the vortex tubes via their end points. Besides advection, such a scheme identically models vortex stretching and reorientation. Calculations with a first-order Euler scheme as well as fourth-order Runge–Kutta scheme have been implemented, with the necessity of using the latter most plainly evident for applications containing solid boundaries where the heightened accuracy is beneficial in resolving the dynamically important motions leading to vortex creation near walls. In the present case such considerations are of lesser importance and the less costly Euler scheme is used for the results shown here.

The vortex filaments follow material fluid elements and thus have a net tendency to stretch. To maintain the accuracy of the discretization, an upper bound, say, h, is placed on the tube lengths $s_i \equiv |\mathbf{s}_i|$ where $\mathbf{s}_i = \mathbf{x}_i^2 - \mathbf{x}_i^1$ is the axial vector along a tube. Tubes for which $s_i > h$ are subdivided into segments of equal length. Where the flow is turbulent vortex stretching leads to the creation of prodigious numbers of tubes. Following Chorin[21,22] vortex loops are removed as they form. The tighter the tolerance in defining a "loop," the less often loops are identified and the larger the number of tubes there are in calculations that have reached equilibrium. The criterion for identifying loops that is used here is based on twice the length of the tubes that are in close proximity to each other. Changes to the loop removal criterion affect the equilibrium number of tubes in a calculation but do not appear to have noticeable effect on such statistics as the mean flow.

The velocity field, $\boldsymbol{U}(\boldsymbol{x},t)$, at a point $\mathbf{x}$ in the flow domain at time t is determined from the cumulative contributions from the vortex tubes together with a potential flow, $\mathbf{U}_p(\mathbf{x},t)$, needed to enforce nonpenetration at solid boundaries. Consequently,

$$\mathbf{U}(\mathbf{x},t) = \mathbf{U}_p(\mathbf{x},t) - \frac{1}{4\pi}\sum_{i=1}^{N} \frac{\mathbf{r}_i \times \mathbf{s}_i}{|\mathbf{r}_i|^3}\Gamma_i \phi(|\mathbf{r}_i|/\sigma), \tag{1}$$

where $\mathbf{r}_i = \mathbf{x} - \mathbf{x}_i$ and $\mathbf{x}_i = (\mathbf{x}_i^1 + \mathbf{x}_i^2)/2$. The ith term in the sum in Eq. (1) represents a simple midpoint rule approximation to the velocity associated with an individual tube as given by the Biot–Savart integral. The smoothing function[12]

$$\phi(|\mathbf{r}_i|/\sigma) = 1 - \left[1 - \tfrac{3}{2}(|\mathbf{r}_i|/\sigma)^3\right] e^{-(|\mathbf{r}_i|/\sigma)^3} \tag{2}$$

is used to desingularize the approximation to the simple Biot–Savart integral and thus prevent unphysical interactions between vortices that are close to being coincident. The magnitude of the numerical parameter σ affects how high up along the singularity in the Biot–Savart function the velocity field is allowed to go before being smoothed to zero. In fact, the effect of ϕ is confined to the region $|\mathbf{r}_i| < 2.34\sigma$ since ϕ is essentially unity beyond this point. The approximate velocity field produced by each individual tube is very accurate outside of its own near field. The use of ϕ compensates for the fact that information about the vorticity within a tube is

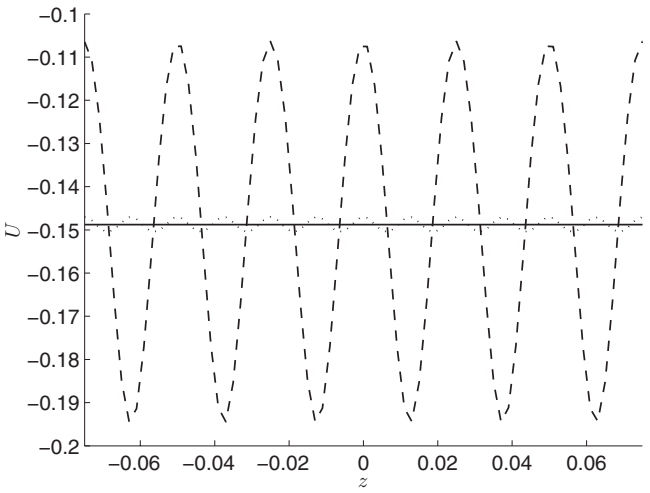

FIG. 1. Evaluation of U velocity component induced on the line $x=0$, $y=0.0125$ by a filament lying on the z axis: —, $h=0.005$; ···, $h=0.0125$; - - -, $h=0.025$.

limited to just the locations of the end points and the amount of circulation, so that the precise form of the detailed, local velocity field cannot be reconstructed. In this aspect the scheme is similar to a LES in the sense that subgrid motions are unknowable. Since h is associated with the magnitude of the velocity induced by individual vortices according to the approximation in Eq. (1), as it diminishes so too does the extent of the near field where local interactions are prone to error, and the overall discretization becomes more accurate. This aspect of the approximation is likely to have had some role in the observation[24] that the use of relatively long tubes can lead to overprediction of the Reynolds stresses. An interesting aspect of this is that once h is set below a threshold the vortex filaments become smooth curves as against a sequence of straight lines with discrete angular changes between the elements. The Reynolds stresses in this case appear to become independent of h and very close to experimental trends. This suggests that errors produced by sudden changes in orientation between adjacent straight tubes may also have something to do with the potential to overpredict the Reynolds stresses. Diminishing h lowers the angles and the errors that go with them.

A more controlled view of the errors produced by h may be seen by applying Eq. (1) to the evaluation of the velocity field corresponding to an infinitely long vortex filament. In particular, consider a vortex filament situated along the z axis whose associated velocity field is independent of z and has nonzero components U and V in the x and y directions, respectively. Subdividing the filament into tubes of equal length and applying Eq. (1) mimics the way in which the velocity is evaluated in the current scheme. Figure 1 shows the U component of velocity computed this way along a line parallel to the z axis at the fixed position $x=0$, $y=0.0125$ for three different values of h. It may be noticed that U is equal to the exact constant value (i.e., independent of z) when the filament is subdivided into short tubes with $h=0.005$. For large $h=0.25$ there is a noticeable oscillation of the computed velocity that coincides with the relative positions that the evaluation points have with respect to the locations of the

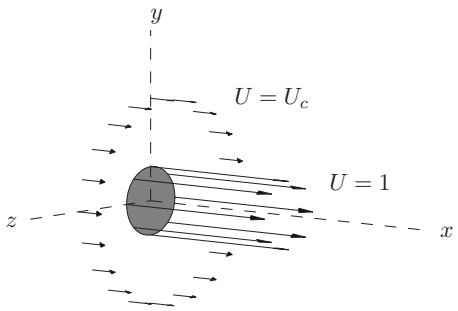

FIG. 2. Geometry of jet simulation.

tubes. For tubes with $h=0.0125$, which equals the distance between the line where the velocity is computed and the filament, the velocity is computed to be nearly constant with just a small oscillation. This establishes the general rule that Eq. (1) is accurate at points further than h from the filaments. Consequently, in any computation for which nearby tubes remain separated by a distance greater than the maximum tube length, the discretization errors associated with Eq. (1) will not be significant. However, neighboring tubes within a distance shorter than the tube length are likely to be affected by errors similar to those in Fig. 1. It may be imagined that this kind of error is exacerbated by sudden changes in orientation of adjacent tubes on the same filament.

Since the magnitude of h is a major factor determining the number of tubes in a calculation and hence its expense, there is a necessary trade-off between accuracy and efficiency in the present simulations very much the way there is in grid-based methods. Fortunately, it appears from this and previous studies that even if it is not practical to work with the optimal h in all cases, nonetheless the statistics and flow properties are well predicted. This suggests that the incidence of very close encounters between vortex tubes for which the local errors may be large are not burdensome in reproducing the correct physics with the filament methodology.

III. NUMERICAL PROBLEM

The flow considered here consists of a round jet with coflow entering an infinite volume at the origin as shown in Fig. 2. It is assumed that length and velocities are scaled by the jet diameter D and inlet centerline velocity U_{CL}, respectively. Consistent with this, the incoming stream is taken to be of the form

$$U(r) = (1 + U_c)/2 - (1 - U_c)/2 \tanh[(r - \gamma_1)/(2\gamma_2)], \quad (3)$$

where $U_c < 1$ is the velocity of the coflow and parameters $\gamma_1 > 0$ and $\gamma_2 > 0$ together determine the location and steepness of the velocity profile at the orifice edge—in this case $r=1/2$. Equation (3) mimics the conditions in a high Reynolds number flow where the potential core occupies most of the inlet and $U(r)$ drops monotonically from 1 to U_c in a thin boundary layer of thickness δ_0 at the edge of the jet. In the present study, the parameter choices $\gamma_1=0.495$ and $\gamma_2=0.001$ are chosen which may be seen to imply that the scale δ_0 is roughly equal to 0.01.

$U(r)$ forms the basis for determining the circulation of circular filaments (i.e., rings) that enter the flow domain at each time step Δt. The boundary layer region at the edge of the orifice, here between $0.5-\delta_0 \le r \le 0.5$, is subdivided into N concentric rings through each of which a new filament enters the flow at each time step. The subdivisions of this region are demarcated by points r_i, $i=0,1,\ldots,N$, with $r_0=0.5-\delta_0$, $U(r_0)=1$ and $r_N=0.5$, $U(r_N)=U_c$. The circulation of the ith filament is $\Gamma_i=[U(r_{i+1})^2-U(r_i)^2]\Delta t/2$. The points r_i are determined with a view toward achieving approximately equal circulation for all filaments. The larger N is the lower the circulation of any one tube and the discretization accuracy is improved. On the other hand, the more rings used in accommodating the incoming flow, the greater the numerical expense. Experience suggests that five layers achieve a reasonable balance between the two counterpoised tendencies.

Each of the circular filaments that enter the flow domain is originally defined as the sides of a polygon inscribed in the unit circle. Typically 20 subdivisions of the circle are made and since for most calculations reported here $h=0.04$, the straight segments immediately subdivide into several vortex tubes as the computations begin. Each of the sides of the inscribed polygon are taken to be a "filament" insofar as the book keeping in the code is concerned even though the sum total of these form one complete physical closed filament. The motivation for this procedure has to do with the need to remove filaments when they travel sufficiently far downstream, as will be discussed below.

A potential flow, as included in Eq. (1) must be introduced to maintain the imposed velocity profile at the entrance nozzle. In essence, the use of the Biot–Savart law in computing velocities makes it necessary to account for the effects of vorticity lying outside the computational domain. For simplicity, the potential flow introduced here is consistent with that produced by a semi-infinite unit diameter vortex tube with unit interior velocity lying upstream of $x=0$. In practical terms it is most efficient to compute this velocity contribution by replacing the vortex cylinder with a unit diameter potential disk placed at the origin with source strengths chosen in such a way as to be consistent with the imposition of the desired $U(r)$ at the inlet. In other words, the flow from the potential disk together with that from the rings near the orifice exit combine to produce the desired inlet velocity distribution.

In this formulation there is no inclusion of a forcing to stimulate the jet to transition to turbulence, as is often necessary in grid-based schemes. In a vortex filament method, the tubes are sensitive to small perturbations intrinsic to the discretization and transition without prompting. To some extent the rate and amplitude of the vortex instability may be curtailed by the use of greater numbers of weaker, shorter vortices that ameliorate the coarseness of the discretization, but in the absence of a viscous diffusion model to smooth perturbations, the occurrence of transition is to be expected. It should be noted that, as will be touched upon later, because of the energy dissipation associated with the use of loop removal at inertial range scales, there is an implied presence of viscous dissipation with an associated Reynolds number, even if the latter is not given explicitly.

For the computational problem to be practical it is necessary to impose a means for limiting the downstream extent of the vortex elements used in representing the jet. By removing vortices at a fixed distance, however, the flow that is inside the computational domain upstream of this point will be affected. Compensation for lost vorticity in this case is made difficult by the fact that the jet velocity decays with distance, so that it not easy to create a simple model of the missing vorticity field. In fact, the least intrusive strategy appears to do nothing and accept the fact that some distortion in the flow properties exists in the region nearest the end plane of the calculation. By monitoring the flow statistics it is possible to trace the induced errors upstream to reveal that part of the solution domain that is affected by the boundary. A similar kind of error was observed in the mixing layer flow[24] where it proved to not be a far reaching effect. In the present case, the effect of the downstream removal of vorticity is felt approximately two jet diameters upstream.

Vortex filaments are removed at a downstream boundary by either of two different approaches. In the first they are removed after all of the component tubes pass a given point, and, in the second, filaments are deleted if any one of their tubes passes a given point. For similar sized computations the former method has an exit plane upstream of that of the latter. On the other hand, the first method has the advantage that the set of vortices in the computational domain is complete. The efficiency with which either of the boundary conditions works depends on how long the removed filaments are in the streamwise direction. In the first case, the longer the filaments are, the more vortex tubes they possess and the greater the burden in un-needed computation beyond the exit plane. For the second boundary condition, there may be a significant part of the computational domain with only a partial population of vortices.

For the jet calculation, the physical vortex rings that enter the flow tend to become very elongated and contain many thousands of tubes by the time they exit the flow domain. The rings are subdivided into numerical filaments as previously discussed so as to reduce the effective lengths of the filaments that are deleted. The penalty for removing parts of the physical vortex rings is that the filaments remaining in the calculation contain free ends for which loop removal becomes ineffective. In fact test computations have demonstrated that the presence of too many loose ends—such as would happen if every tube passing a point was removed from the computation—can lead to unbounded growth in the number of tubes due to the failure of loop removal. The approach adopted here is a compromise between the two extremes: it permits some tolerance of filaments having free ends so as to reap the advantage of reducing the streamwise extent of the departing filaments, but it does not include so many as to hamper the effectiveness of loop removal.

It may be noted that a separate issue in having free ends is that at each of these points the zero divergence condition of the vorticity field is violated. This presumably produces additional local errors besides those associated with the Biot–Savart evaluation and the perturbations produced by

loop removal. While it is possible to modify the effective vorticity at the free ends so that zero divergence is maintained,[12] the potential benefit of such an alteration does not appear to be sufficient to warrant the greater numerical expense entailed in its implementation.

The presence of a significant positive jet coflow means that the number of vortices appearing in a calculation can be expected to reach equilibrium since the support of the vorticity field is finite in this case. In addition, the higher the coflow, the smaller the residence time of tubes in the flow domain and the longer the computational domain can be made for the same number of tubes. The calculations here include coflows $U_c=1/10$, 1/5, 1/4, 1/3, and 1/2 or, in terms of the parameter $\Lambda \equiv (1-U_c)/U_c$ representing the ratio of the initial velocity excess to the coflow speed, the cases considered have $\Lambda=9$, 4, 3, 2, and 1. Both of these means of characterizing the simulations will be used in the sequel. The higher the value of Λ, the closer the coflowing jet is to a traditional round jet. The streamwise extent of the simulations varies from $L=5.25$ for $U_c=1/10$ to $L=15.8$ for $U_c=1/2$. For most runs $h=0.04$, $\Delta t=0.04$, and contain up to 13×10^6 vortices at equilibrium. A limited simulation was also made for the 1/3 coflow case with $h=0.015$ and 20×10^6 vortices at equilibrium.

The simulations were performed primarily on an HP Alpha EV7 parallel supercomputer at the Pittsburgh Supercomputing Center. The most time consuming aspect of the algorithm is the evaluation of velocities at the locations of the N vortices via Eq. (1). The nominal $O(N^2)$ cost of this step is reduced to $O(N)$ via a parallel implementation of the adaptive fast-multipole method,[25] thus creating the opportunity to use large numbers of vortices. Mean statistics for the jet simulations are taken from velocity records accumulated over a nondimensional time interval of 20–40 encompassing 500–1000 time steps. For a case with approximately 12×10^6 vortices at equilibrium and using 16 processors, the computations require between 2.5 and 5 days for execution. Such timings compare favorably to numerical costs reported for grid-based LES simulations (e.g., Refs. 2 and 9).

Depending on the coflow, from 1×10^6 to 3×10^6 additional vortex tubes are needed to resolve each additional jet diameter downstream in the fully turbulent region of the jet. For typical computer systems, this represents a significant obstacle in extending the calculations to very long distances. A practical consequence for the present study is that the cases with the lowest coflows and hence shortest computational domains may show a comparatively greater influence of the downstream boundary than the other simulations.

It is interesting to note that the computation of jet flows scaled on orifice diameter is a substantially more ambitious calculation than a planar shear layer scaled to unit width. In fact, the jet inlet has a shear layer of length π that is more than three times longer than that of the plane shear layer. Unless unusually large computer resources are available, this means that a choice has to be made between choosing large L or small h. In this study, h is taken to be in a range that is larger than it would be if dictated solely by a desire to eliminate discretization errors. By this step it has been possible to calculate the jets well into the turbulent region.

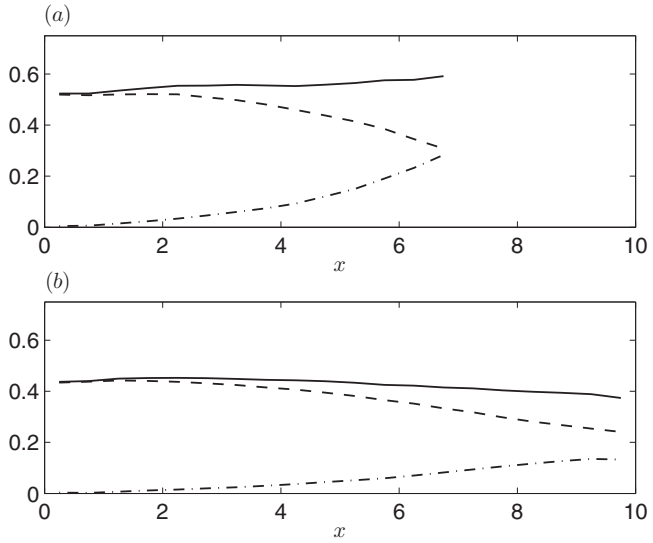

FIG. 3. Streamwise decomposition of J. —, J; - - -, contribution from $\bar{U}$; - · -, contribution from $\overline{u^2}$. (a) $U_c=1/5$; (b) $U_c=1/3$.

IV. VELOCITY STATISTICS

The coflowing jet has been well studied in physical experiments and many flow statistics are available with which to assess the quality of the vortex filament simulations. Of particular interest is seeing if the method can capture trends that arise from changes in the coflow since these point toward the effectiveness of the approach in responding to subtle physical differences that are not readily modeled.

To set the stage for making comparisons it is helpful to first consider fundamental quantities categorizing jets such as the momentum excess,

$$J \equiv 2\pi \int_0^\infty \overline{(U-U_c)U} r dr$$

$$= 2\pi \int_0^\infty (\bar{U}-U_c)\bar{U} r dr + 2\pi \int_0^\infty \overline{u^2} r dr, \tag{4}$$

where $\overline{u^2}$ is the streamwise Reynolds stress, and the mass flux

$$M \equiv 2\pi \int_0^\infty (\bar{U}-U_c) r dr, \tag{5}$$

that may be calculated at each fixed streamwise location. Integration of the momentum equation on planes normal to the axial direction suggests that, barring any significant viscous effect or change in mean pressure, J is constant independent of x. In this case, the momentum radius, $\theta \equiv \sqrt{J}/U_c$, is useful in a number of contexts for characterizing the jet behavior independent of conditions specific to a particular case. According to the second equality of Eq. (4), J may be decomposed into the sum of a part depending on the mean velocity and a contribution from the streamwise Reynolds stress. Figure 3 shows an evaluation of Eq. (4) including the two terms in its decomposition for the cases with $U_c=1/5$ and 1/3. In both plots in the figure the approximate constancy of J is evident with the small variability most likely an arti-

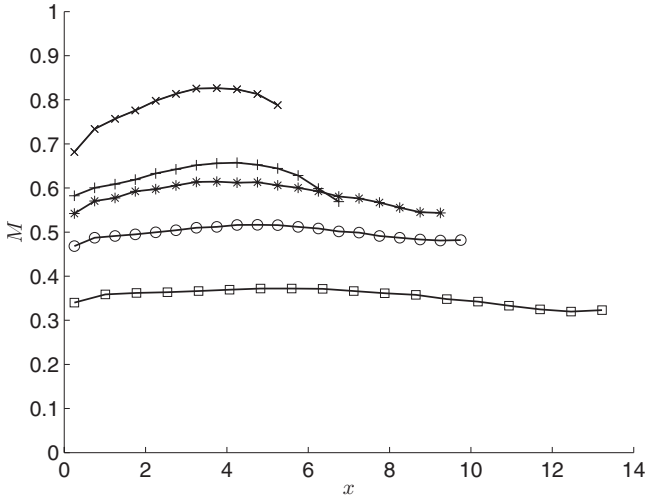

FIG. 4. Streamwise variation of M for different values of U_c: ×, 1/10; +, 1/5; *, 1/4; ○, 1/3; □, 1/2.

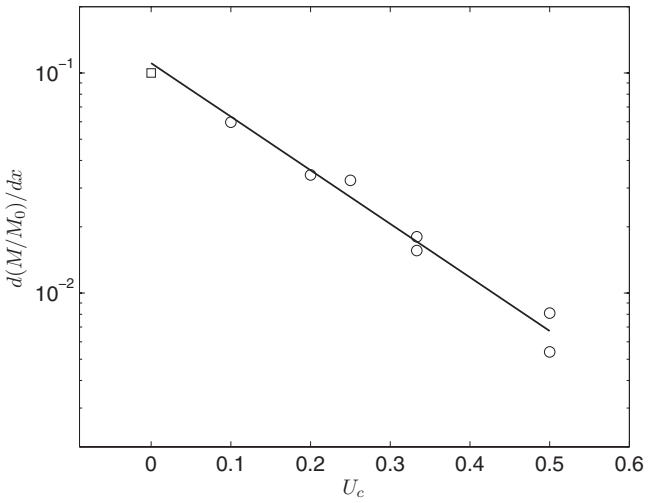

FIG. 5. Dependence of entrainment on speed of the coflow: □, from Liepmann and Gharib (Ref. 26); ○, computations.

fact of the limited averaging and possibly the influence of the downstream boundary condition.

According to the figure, from initially laminar conditions in which the momentum excess is entirely contained within the mean field, the contribution from the Reynolds stress grows finally accounting for a significant share of the total momentum excess. The growth of the Reynolds stress contribution reflects the transition to turbulence in the jet—a central part of which is the gradual diminishment of the laminar potential core with streamwise distance, as will be observed in detail below. Some tendency toward an equilibrium in the division of J between the mean field and the Reynolds stress terms appears to be occurring for the 1/3 coflow. In both cases the streamwise extent is not long enough to see what the final trends will be. Between the two cases it appears that for the smaller coflow the Reynolds stress grows to account for a majority of the velocity excess. The results shown in Fig. 3 fit in with similar analyses of the other coflows. Until such time as substantially longer jets are computed it is not possible to reach stronger conclusions about the asymptotic behavior of the momentum excess or to perhaps make comparisons with experiments.

The mass flux, shown in Fig. 4, rises initially and, in accordance with the finite and relatively modest length of the computational domains, reaches a maximum and subsequently falls. The simulations with the smallest coflows see the greatest rise in mass flux indicating the presence of stronger transitional vortices that cause greater entrainment of fluid into the jet. At the same time, since these are the shortest of the simulations, they are seen to undergo a relatively rapid decrease in mass flux as the effects of the truncation of the vorticity field are felt. Liepmann and Gharib[26] made a careful study of the normalized entrainment $d(M/M_0)/dx$, where $M_0 \equiv M(0)$, in the near field of a round jet without coflow. Assuming that near the orifice the results for M in Fig. 4 are untainted by downstream effects, then it is interesting to examine the consistency between the observed entrainment in a round jet and the trend in the present data as it changes with the coflow.

According to Fig. 4, M is linear near $x=2$ for each of the coflows considered, so that it is possible to get an unambiguous estimate of the slope by least-squares fitting a straight line in each case. A cursory examination of the observed dependence of the predicted entrainment on U_c suggests that it is exponential which motivates the semilog plot of entrainment versus U_c given in Fig. 5. Included in the figure is a value for the round jet[26] which is seen to be fully consistent with the behavior seen in the simulations. Whether or not the result shown in this figure is amenable to explanation in terms of the dynamics of the near field vortices remains to be seen.

A representative example of the simulated mean velocity field across the jet is shown in Fig. 6 corresponding to the 1/3 coflow solution at $x=8.75$. The computed, normalized mean velocity, $\bar{U}_n(x,r) \equiv (\bar{U}(x,r) - U_c)/\Delta U(x)$, where $\Delta U(x) \equiv \bar{U}(x,0) - U_c$, is compared to experimental values[27] as well as the Gaussian form $e^{-(r/\delta)^2}$. Here, the length scale δ

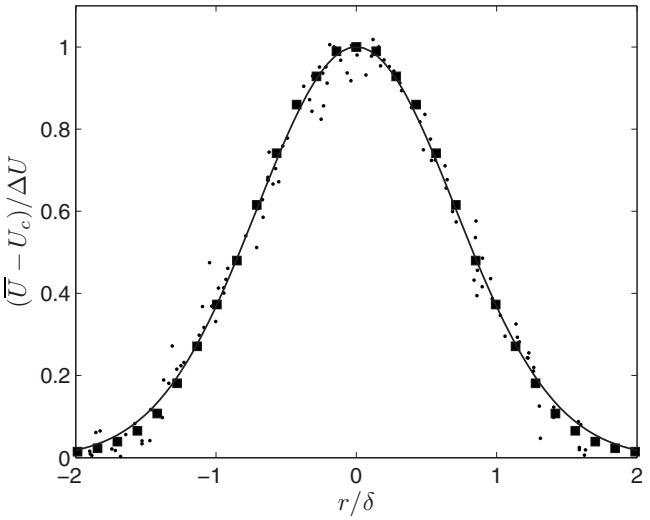

FIG. 6. $(\bar{U} - U_c)/\Delta U$: ●, data of Chu *et al.* (Ref. 27) at several values of $\Lambda \geq 10$; ■, computed with $\Lambda = 2$ at $x=8.75$; —, $e^{-(r/\delta)^2}$.

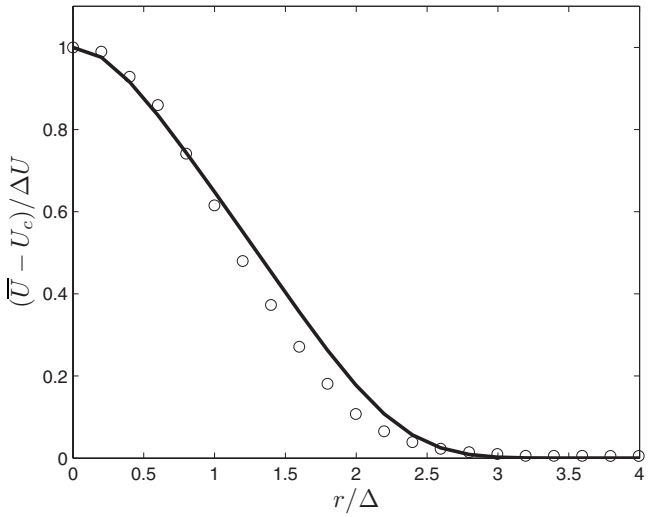

FIG. 7. $(\bar{U}-U_c)/\Delta U$. ○, computed with $\lambda_J=2$ at $x=8.75$; —, Eq. (8) from Nickels and Perry (Ref. 28) fitted to data with $\lambda_J=2$, 10, and 20 at $x=30$.

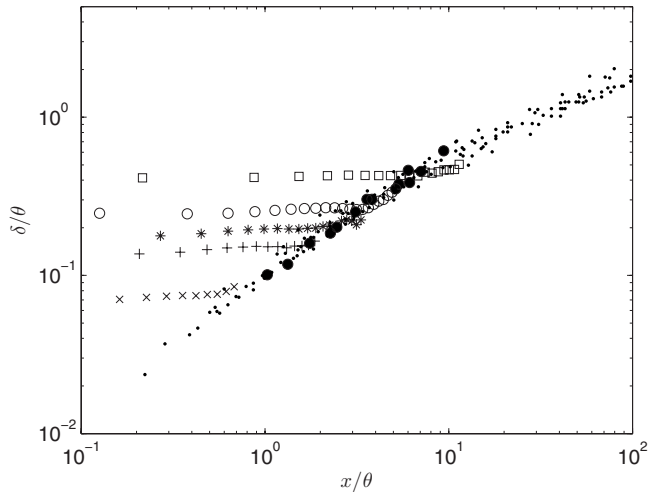

FIG. 8. Streamwise dependence of δ. Computations at different U_c: ×, 1/10; +, 1/5; *, 1/4; ○, 1/3; □, 1/2. ●, experiments by Chu *et al.* (Ref. 27); ·, data assembled by Davidson and Wang (Ref. 29).

is determined as the value of r when $\bar{U}_n=e^{-1}$. There appears to be little doubt that the computed mean velocity is consistent with a Gaussian profile, a result which holds equally well at any of the streamwise positions in this and the other coflows where the flow is fully turbulent.

A more general definition of the jet width,[28] that is not specific to a Gaussian profile, may be defined via

$$\Delta \equiv \sqrt{\int_0^\infty (\bar{U}-U_c)r^2dr \Big/ \int_0^\infty (\bar{U}-U_c)dr}. \tag{6}$$

In the case that $\bar{U}$ is Gaussian, a calculation shows that

$$\Delta/\delta = 1/\sqrt{2}. \tag{7}$$

Nickels and Perry[28] fitted their measured values of $\bar{U}_n$ for $\Lambda=2$, 10, and 20 to the empirical function

$$e^{-0.677\eta_m^2+0.364\eta_m^3-0.121\eta_m^4}, \tag{8}$$

where $\eta_m \equiv r/\Delta$, showing excellent agreement and collapse of the data. Figure 7 compares the same computed profile shown in Fig. 6 with Eq. (8). The agreement in this case is not quite as good as with the Gaussian in Fig. 6, suggesting that at least for the present study, a Gaussian is the more likely behavior of the mean velocity field. The reason for the discrepancy between experiments is not apparently known.

Regardless of the details of the mean velocity distributions, the predicted scales for the simulated jets show a substantial agreement with both sets of experiments as is indicated in Fig. 8 for δ and Fig. 9 for Δ. In particular, it is seen that the computed values merge smoothly into the physical measurements after the transitional region. The data used in the comparison for the scale δ include some measurements of Chu *et al.*[27] and a sampling of results from many different experiments assembled by Davidson and Wang.[29] The data in this case undergo a transition from slope 1 at small x/θ to slope 1/3 at large values. The results from the simulations appear to be largely compatible with this nonlinear trend.

Since the velocity profiles at the orifice are not Gaussian, it is interesting to see at what point Gaussianity is achieved. Some idea of where this occurs is furnished by Fig. 10 containing a plot of the streamwise variation of the ratio Δ/δ for the different coflows. Despite some obvious noise in the data, part of which is presumably due to the downstream boundary condition, there seems to be a clear trend toward the Gaussian value of $1/\sqrt{2}$ at locations in the turbulent field immediately after the end of the potential core region.

Accurate prediction of the length of the potential core region in a traditional round jet represents a significant challenge for LES techniques.[2] The additional influence that a coflow may have on this length makes the problem that much more difficult. A quantitative indication of the core region for any particular jet may be deduced from plots of the velocity excess defined as $\Delta U/U_c$ since this is constant through the core region before subsequently dropping thereafter. Results for the velocity excess for the present compu-

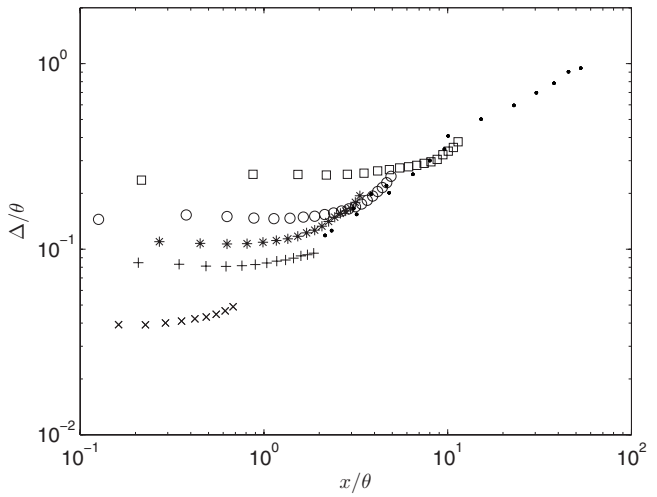

FIG. 9. Streamwise dependence of Δ. Computations at different U_c: ×, 1/10; +, 1/5; *, 1/4; ○, 1/3; □, 1/2. ·, experiments from Nickels and Perry (Ref. 28).

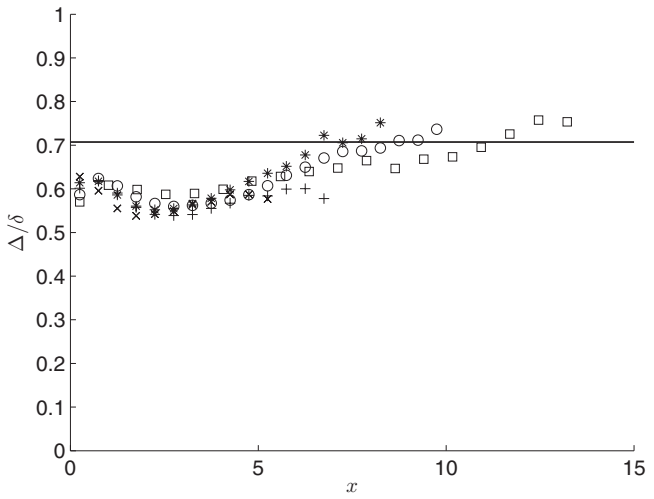

FIG. 10. Variation of Δ/δ with x. Computations at different U_c: ×, 1/10; +, 1/5; *, 1/4; ○, 1/3; □, 1/2. The horizontal line is at $1/\sqrt{2}$.

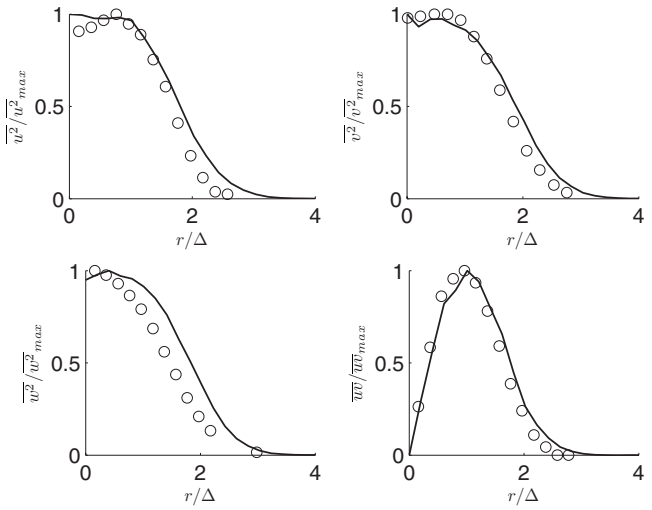

FIG. 12. Reynolds stress components. ○, experiments (Ref. 28) with $\Lambda=2$; —, computations with $\Lambda=2$ and data averaged between $3.7\leq x/\theta\leq 4.9$.

tations are plotted in Fig. 11 together with an agglomeration of experimental measurements from Chu *et al.*[27] and Nickels and Perry.[28] With the exception of a small under prediction for the smaller coflows the extent of the core region is well accounted for. While the effect of the downstream boundary may have some influence on the discrepancies in this figure, they also may reflect differences in the upstream boundary conditions between the simulations and experiments as well as the strong perturbative effect of the vortex tube representation that leads to a relative rapid transition. Both of these kinds of influences have been seen previously in DNS jet simulations by Boersma *et al.*[30] In all cases the decay of centerline velocity immediately after the potential core is seen to be consistent with experiments both in slope and in the fact that it collapses to a single curve.

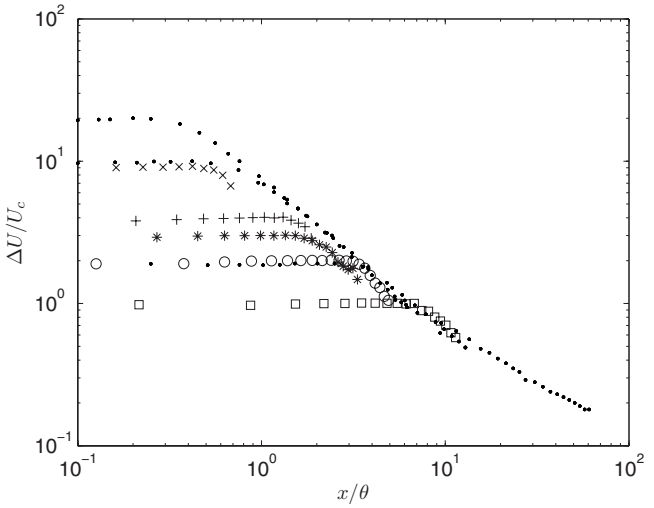

FIG. 11. Streamwise dependence of nondimensional velocity excess. Computations at different U_c: ×, 1/10; +, 1/5; *, 1/4; ○, 1/3; □, 1/2; ·, experiments as given by Chu *et al.* (Ref. 27) and Nickels and Perry (Ref. 28).

V. REYNOLDS STRESSES

It has been observed,[28] particularly insofar as amplitudes are concerned, that there is considerable variability from one experiment to another in the normalized Reynolds stresses such as $q\equiv\overline{u^2}/(\Delta U)^2$. Evidently, it is necessary to mimic the details of a specific facility (e.g., upstream turbulence levels, nozzle design) in order make precise comparisons between numerical predictions of Reynolds stresses and data from physical experiments. For the present study there also tends to be a significant discrepancy between the downstream locations in the self-similar region where the Reynolds stresses are often measured in experiments and the points further upstream where they are computed in this study. Other factors that inhibit direct comparison between experiment and computation are differences in Reynolds number and possibly the use of vortex discretizations with h larger than optimal. Nonetheless, by focusing on some of the more general properties of the Reynolds stresses it is possible to gain some sense of the intrinsic physicality with which they are accounted for by the vortex simulation.

The Reynolds stress amplitude measured in Ref. 28 has $q\approx 0.08$ which is in the low end of observations and approximately half the amplitude of the present simulations. Useful comparisons can be made in this case by scaling by the local maxima as shown in Fig. 12 where separate plots are given of the streamwise, radial, and azimuthal normal Reynolds stress components as well as the shear component. To obtain smoother results, the numerical curves represent averages over values taken between $3.7\leq x/\theta\leq 4.9$. The radial scaling uses Δ averaged over the same interval and it is seen that the computations match the trends closely. The most significant difference here lies in the greater isotropy of the computations in which, unlike the experiments, $\overline{v^2}$ and $\overline{w^2}$ are almost identical. For this reason the calculated $\overline{w^2}$ appears to be slightly higher than the trend in the data. The heightened isotropy of the computations is likely to be a by-product of the use of a relatively large h.

Nickels and Perry[28] showed that $\overline{|uv|}/\overline{|uv|}_{\max}$ has a ten-

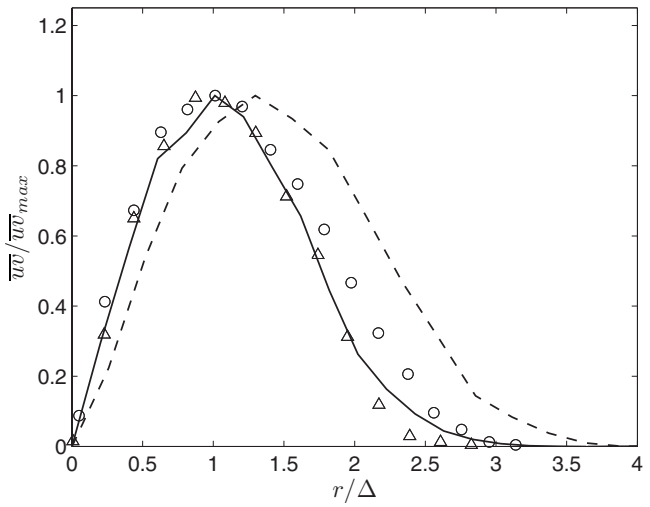

FIG. 13. Shear component of Reynolds stress. △, like a small-excess jet (Ref. 28); ○, like a free jet (Ref. 28). Computations: —, $U_c=1/3$; - - -, $U_c=1/5$.

dency to spread wider near the origin where ΔU is relatively large than it does far downstream where the velocity deficit is small. A similar trend is found to occur here as shown in Fig. 13 where the computed normalized shear stress for the 1/5 coflow is seen to be spread wider than that for the 1/3 coflow. It should be noted that in this figure the plotting depends on the predicted value of Δ that may to some extent, particularly for the 1/5 coflow case, be influenced by proximity to the downstream boundary.

A different look at the normal streamwise Reynolds stress is given in Fig. 14 for data from Antonia and Bilger[31] that has considerably larger amplitude than that in Ref. 28. In fact, the computed stresses in this case are similar to the experiments in regards to both magnitude and other qualitative features. The length scale δ_h used in Fig. 14 is the true velocity half-width defined by the requirement that $\bar{U}_n(x,\delta_h)=1/2$. Shown in the figure is the computed Reynolds stress distribution for $U_c=1/3$ at position $x/\theta=3.2$ in the vicinity of the end of the potential core and at $x/\theta=3.9$ near the downstream boundary. In both cases and most markedly in the first position, the Reynolds stress has a local minimum on the jet axis. This is qualitatively similar to the experimental measurements that are taken at the same value of Λ but very much more jet diameters downstream. The numerical results are seen to be spread slightly further than the data, an effect that could be tied to differences in δ_h among a number of other factors.

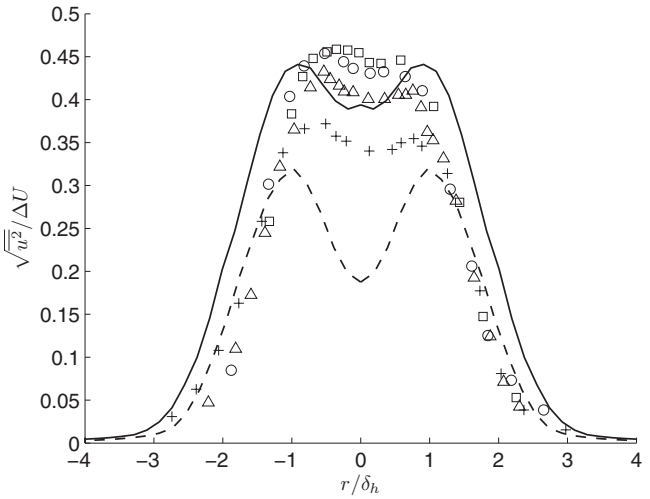

FIG. 14. rms streamwise velocity scaled by velocity excess. Symbols: data from Antonia and Bilger (Ref. 31) at several locations in jet with $\Lambda=2$. Computations with $\Lambda=2$: - - -, $x/\theta=3.2$; —, $x/\theta=3.9$.

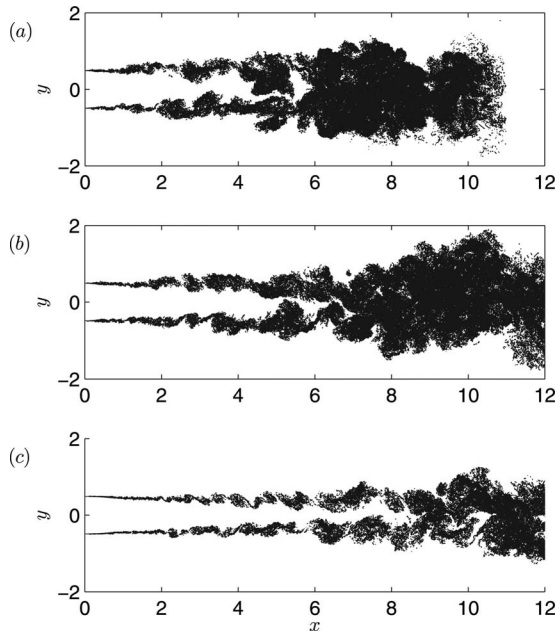

FIG. 15. Vortex elements intersecting within 0.01 of the x-y plane. (a) $U_c=1/4$; (b) $U_c=1/3$; (c) $U_c=1/2$.

VI. VORTICITY FIELD

The population of vortex filaments that comprise the simulated jets provides a direct view of the underlying vortical structure of the flow field that is helpful in understanding its development through transition to a turbulent state. It is most useful to consider views of the vortex tubes selected according to their having an end point within narrow slices of the flow volume. For example, vortices with end point $\mathbf{x}_i^1=(x_i^1,y_i^1,z_i^1)$ satisfying the condition $|z_i^1|\leq 0.01$ provide a view of the jet structure on the x-y plane through the central axis. Figure 15 shows these collections of vortices for the three coflows 1/4, 1/3, and 1/2. From this perspective the vortical shear layers leaving from the orifice are plainly visible as they frame the potential jet core at the center.

The shear layers progress through a transition that is very similar if not equivalent to that of a planar shear layer. Vortical structures, essentially ringlike roller vortices with connecting streamwise rib vortices, form, grow, and merge out of the incipient shear layers and represent the primary mechanism by which the potential core of the jet gradually erodes giving way to a fully turbulent state.[26,32] As in experimental visualizations in round jets[33] a noticeable asymmetry develops to the vortex structure on either side of the jet.

Exactly how far downstream the core region persists for a given coflow is tied to the properties of the vortical structures produced in the shearing. For the 1/4 coflow shown here and the smaller coflows that were studied, the potential core extends to somewhat beyond six diameters downstream and fits in with the core lengths in a range up to approximately 6 seen in the classical round jet with no coflow.[27] For the higher coflows, it is clear from the figure that there is a significant increase in the length of the coflow region.

The initial development of the jet shear layers immediately downstream of the orifice follows a sequence of events that is controlled somewhat by the discrete representation of the flow in terms of filaments and tubes. In particular, as observed in the planar mixing layer study,[24] the initial perturbations of the filaments are constrained to occur at the junctions between straight tubes. In the present case, this tendency is heightened by the systematic arrangement of the tubes in the vortex rings that enter the computational domain. In particular, the polygonal structure to the rings contains discontinuous changes in tube orientation that act as perturbations to the axial symmetry, in addition to whatever biases are contained in Eq. (1). The footprint of the polygonal structure is for the most part not evident beyond one diameter from the orifice where the shear layer thickens as seen in Fig. 15. Beyond this point the azimuthal distribution of rib vortices, for example, does not show any connection to the artificial structure imposed at the inlet.

Figure 15 is useful for seeing how the length of the core region determined by the growth of the shear layers is connected to differences in the vortical transition corresponding to different coflows. Clearly, for the relatively low coflow of 1/4, the growth rate of the turbulent vortices is much faster than the high coflow $U_c=1/2$ case with the result that the potential core is closed much earlier. It may also be seen that the relatively weaker vortices in the latter case undergo substantially more vortex mergers than the lower coflow. For example, a visual inspection of Fig. 15 suggests no more than five pairings for the 1/4 coflow and at least ten for the 1/2 coflow.

A closer look at the three-dimensional (3D) structure of the transition is provided by Figs. 16 and 17 showing a view from the top and bottom, respectively, of the vortex filaments contained in the top and bottom halves of the streamwise region $2 \leq x \leq 4$ for the $U_c=1/3$ jet. For clarity, only every third filament is displayed in these figures. These images may be directly correlated with the structure seen in the center illustration of Fig. 15. In particular, the sequence of braid, roller, braid, and roller events in the lower shear layer centered at the points $x=2.4$, 2.75, 3.1, and 3.5, respectively, is reproduced magnified in Fig. 17. Matching these up with the view in Fig. 16 establishes that the turbulent roller vortices are more or less ringlike and contain streamwise rib vortices of an equivalent scale. At the location visualized here the large roller and rib vortices are the direct result of the vortex merger process in the growing shear layers. The roller vortex at 2.75 in Fig. 17 gives a good indication of how roller vortices are perturbed by the wrapping around them of streamwise rib vortices.

An end-on view of the vortices in the 1/3 jet at the four

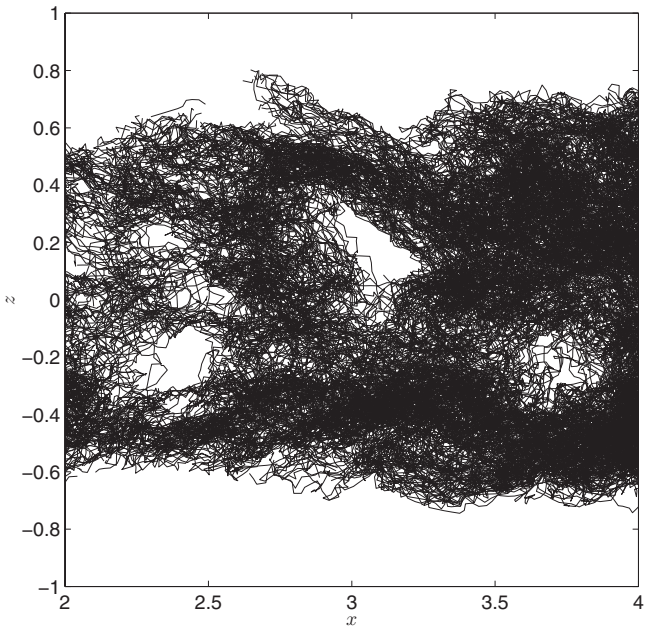

FIG. 16. Roller and rib vortices in the top half-plane viewed from above for 1/3 coflow jet in Fig. 15.

specific streamwise locations referenced above are shown in Fig. 18. It is interesting to note the difference in the thicknesses of the vortex layers between the left and right images corresponding to the braids and rollers, respectively. This dichotomy is similar to that seen in dye marker viewed in braid and roller positions in a transitioning jet.[26] The lobes represent streamwise vortices and vortex pairs arrayed around the jet perimeter. As in Figs. 16 and 17, the rib vortices often extend between several of the images in Fig. 18. As mentioned in regards to Fig. 17 the ribs are seen to have

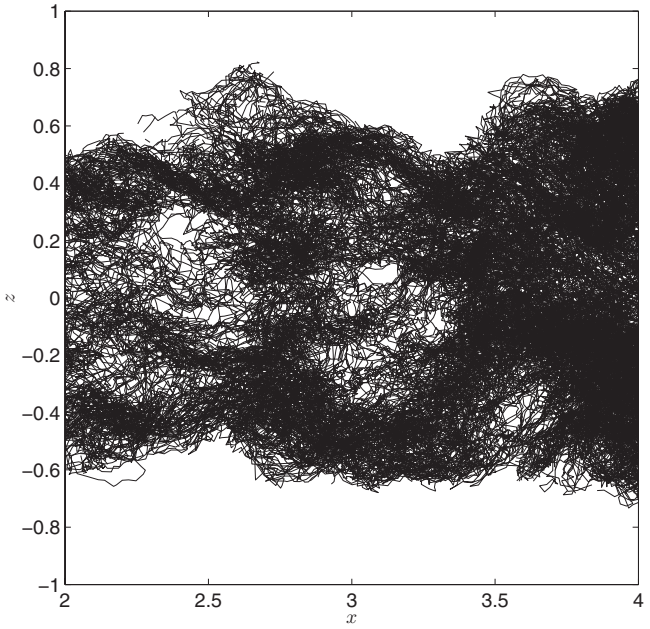

FIG. 17. Roller and rib vortices in the bottom half-plane viewed from below for 1/3 coflow jet in Fig. 15.

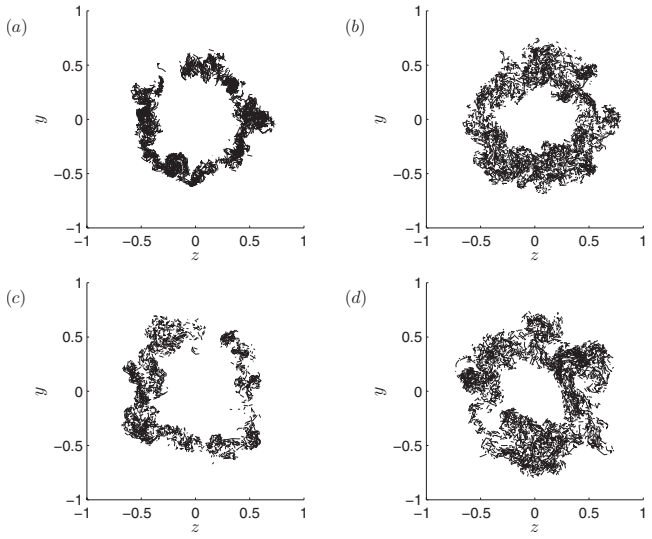

FIG. 18. End-on view of vortex elements for the $U_c=1/3$ jet: (a) $x=2.4$ (braid); (b) $x=2.75$ (roller); (c) $x=3.1$ (braid); (d) $x=3.5$ (roller).

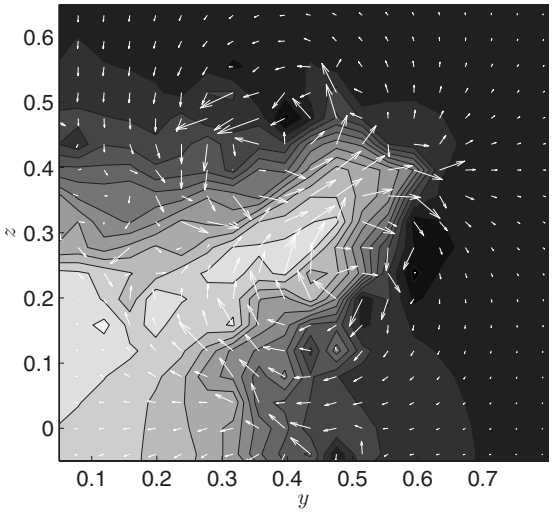

FIG. 20. Contours of axial velocity U together with velocity vectors for the same event as in Fig. 19. U ranges from 1 (lightest shading) to 1/3 (darkest shading).

a significant effect in distorting the circularity of the roller vortex rings. The end result is to create the lobed appearance of the vortices in the cross sections.

Figure 19 is a detail of a particularly well formed vortex lobe that is composed from counter-rotating rib vortices. The vortex elements in the figure intersect the thin volume within $x=3.5\pm0.025$ (at a different time than in Fig. 18). Also plotted are velocity vectors showing the projected motion in the plane. It is evident that the vortices induce a significant outflow as well as potential motion outside the support of the vorticity itself[34] that would lead to entrainment of the fluid into the jet. The kind of motion in this figure is not unlike that described in experiments[26] and is a central facet of the motion that produces the lateral spread of the jet. Figure 20 shows contours of the streamwise velocity together with the planar velocity vectors that leave little doubt that the action of the streamwise vortices is to both cause the lateral ejection outward of high speed fluid that is initially located near the axis of the jet as well as to entrain the slower moving coflow toward the jet center.

After transition and the end of the potential core, Fig. 15 shows that the fully turbulent jets acquire structure encompassing the full jet width. This has the appearance of a sinuous motion built up from agglomerations of the large vortices produced at the end of the vortex merger and growth. Presumably this structure persists downstream some distance before forming the kinds of structures that define the self-similar region.

Another aspect of the jet structure is revealed by looking at individual vortex filaments at different locations within the jet. These are the physical filaments representing the union of the numerical filaments forming complete vortex rings entering the computational domain. A 3D view of filaments beginning at the orifice for the 1/5 coflow is given in Fig. 21 with corresponding images from an end-on perspective in Fig. 22. For the filament near $x=1$ the azimuthal perturbations going around the ring are seen to also have a significant streamwise component that includes deformation both upstream and downstream corresponding to inward and outward deviations from the nominal position. At this point the imprint of the initial polygonal structure is reflected in the number of distortions spread around the ring.

Beginning near $x=2$ and partially evident in the end-on view in Fig. 22(c) the influence of the inlet structure has

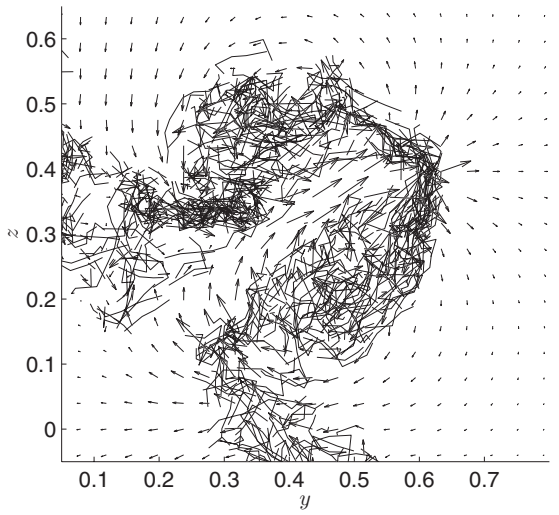

FIG. 19. Detail of velocity vectors and vortical structure on plane $x=3.5$ at a fixed time in the 1/3 coflow simulation.

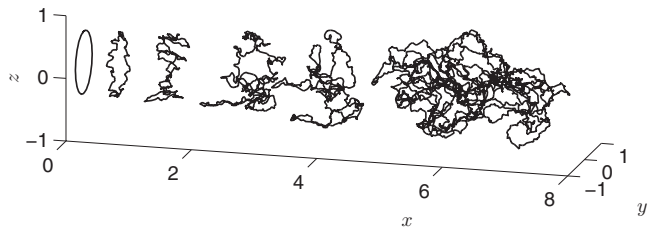

FIG. 21. Individual vortex filaments in the 1/5 coflow jet.

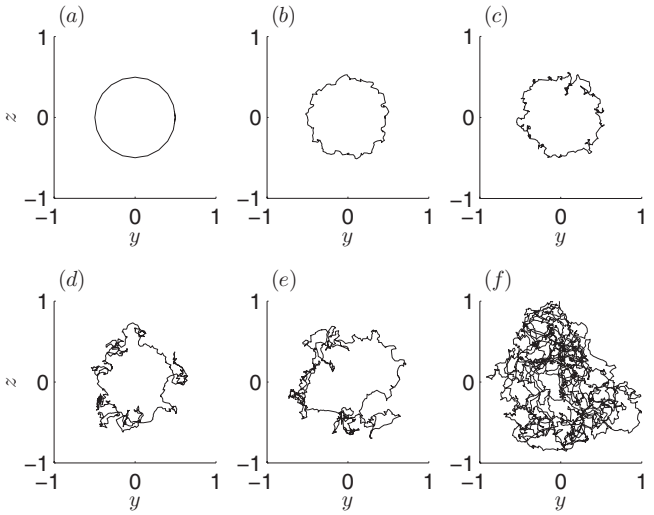

FIG. 22. End-on views of the vortex filaments shown in Fig. 21. (a)–(f) correspond to the vortices in increasing x.

been supplanted by larger scale disturbances associated with the growth of the rib vortices. Here there begins long extensions in the streamwise direction, culminating in the fourth and fifth images that are in the late stage of transition. The filaments in this case wind through the transitional vortex structure as seen in Figs. 16 and 17. The final vortex filament, containing thousands of individual tubes, is entirely in the fully developed part of the jet. This covers a substantial streamwise region as well as the entire jet cross section. It may be assumed that loop removal has been felt in the elimination of finer scale windings of the vortex filaments in this and the other filaments in Figs. 21 and 22.

VII. REYNOLDS NUMBER

As noted previously, the coflowing jet begins to transition to a turbulent state largely as the end result of perturbations intrinsic to the discrete representation of the vorticity field. In this there is no explicit use of a viscosity tied to a Reynolds number. Moreover, while a Reynolds number may be implicit in the incoming flow—since boundary layers containing vorticity are put in place at the edge of the orifice—it makes no explicit appearance in the simulation. On the other hand, the simulation relies on loop removal to supply what amounts to spatially intermittent energy dissipation and where there is dissipation there must be a viscosity and hence local and global Reynolds numbers. The goal now is to estimate the Reynolds numbers for the jet flow, both because of their intrinsic interest but also to gain some insight into how the choice of numerical parameters associated with loop removal, primarily vortex length, affects these values. This should be useful in problems containing solid boundaries where a Reynolds number is explicitly assigned and where one would like it to be consistent with the Reynolds number produced by the turbulent vortices.

A means of estimating Reynolds number follows from several universal properties of homogeneous and isotropic turbulence that are herein assumed to prevail locally in an approximate sense in the jet flow. In particular, the one-dimensional (1D) Kolmogorov inertial range spectrum,

$$E(k) = C_K \epsilon^{2/3} k^{-5/3}, \tag{9}$$

is assumed to apply, where k is the wave number and $E(k)$ is the energy spectrum density. A distillation of empirical results from a diverse group of experiments[35] suggests that 0.53 is the best estimate for the Kolmogorov constant C_K with the qualification that the Reynolds number be sufficiently large. For example, DNS of isotropic turbulence[36] suggests that $C_K=0.60$ may be more appropriate if $R_\lambda<100$. Here, the Reynolds number $R_\lambda=\sqrt{\overline{u^2}}\lambda/\nu$; $\overline{u^2}$ is the streamwise normal Reynolds stress and λ is the longitudinal Taylor microscale. A preliminary calculation has shown that for either choice of C_K it turns out that R_λ is below 100 so that the following discussion is predicated on the use of $C_K=0.60$. In any event, use of a different value of this parameter leads to relatively small quantitative changes in the results without affecting the overall conclusions.

To the extent that a $-5/3$ law of the form $C_1 k^{-5/3}$ with constant C_1 is observed locally in the jet simulation, then the dissipation rate can be estimated from

$$\epsilon = (C_1/C_K)^{3/2}. \tag{10}$$

In fact, consistency of the vortex simulation with Eq. (9) was reported previously[23] and is also found to be present in the jet simulations considered here, so a determination of ϵ can be made as a first step toward acquiring a Reynolds number.

A further assumption may be made that the isotropic identity

$$\epsilon = \frac{15\nu\overline{u^2}}{\lambda^2} \tag{11}$$

has at least some approximate local validity in relating the dissipation rate to λ and $\overline{u^2}$. In this case, rearranging Eq. (11) and applying the scaling used in the jet problem yields

$$R_e = \frac{U_{\mathrm{CL}} D}{\nu} = \frac{15\overline{u^2}}{\lambda^2 \epsilon}, \tag{12}$$

and a further calculation gives

$$R_\lambda = \frac{u'\lambda}{\nu} = u'\lambda R_e, \tag{13}$$

where $u' \equiv \sqrt{\overline{u^2}}$. In this way, an approximate determination of Reynolds numbers can be achieved.

For the purposes of the present study, the Reynolds number associated with the $U_c=1/5$ simulation at $x=6.25$ and the 1/3 coflow simulation at $x=8.25$ are considered. These are representative of the results for simulations at the other coflows. To provide further contrast the simulation with 1/3 coflow is taken to have $h=0.015$ instead of the nominal $h=0.04$ used in the 1/5 coflow calculation.

An estimate of ϵ and the other quantities pertaining to Eqs. (12) and (13) can be had from velocity data obtained on compact regions of short streamwise extent. Appropriate to the jet, whose mean field is axisymmetric, the velocity data are computed on a cylindrical mesh whose appearance on a cross plane is shown in Fig. 23. The mesh in the figure con-

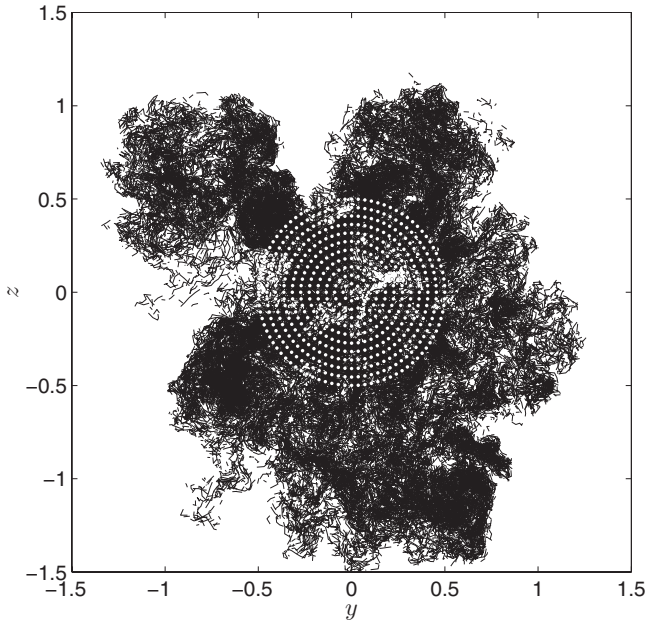

FIG. 23. End-on view of the grid used in obtaining velocity statistics superimposed on the vortex filaments within a thin slice of the 1/5 coflow jet at $x=6.25$.

sists of 12 concentric circles of equally spaced points with the outermost layer at $r=0.5$. Shown with it are the vortex tubes in a thin slice $6.24 \le x \le 6.26$ at one instant of time of the 1/5 coflow jet. At this streamwise location, more than six diameters from the origin, there is significant intermittency as is evidenced by voids in the vortex field that penetrate to within $r=0.5$ of the jet axis. The grid in the figure is limited to a radius of 0.5 so as to avoid having to take intermittency into account in the analysis: it is assumed that the flow is continuously turbulent within the central core of the jet covered by the mesh out to $r=0.5$.

The streamwise discretization of the grid in Fig. 23 consists of 201 points extending a distance 0.2 fore and aft of the plane $x=6.25$. A similar mesh centered on 8.25 is used for the 1/3 coflow case. The spacing of points, $\Delta x=0.002$, is more than adequate to ensure a fine-grained representation of the velocity traces. To obtain statistics at any fixed r, averaging is performed over the data on fixed cylindrical shells of grid points: 57 time steps separated by $\Delta t=0.4$ representing an elapsed time of 22.4 is used for the 1/5 coflow data and 35 time steps covering an elapsed time of 13.6 for the 1/3 coflow. Points further from the center in the mesh are necessarily better averaged than those closer in. In view of the minimal amount of data at $r=0$, averaging is not done at this point.

Figure 24 gives representative views of the 1D streamwise energy spectrum at $r=0.32$ for the two coflows. These apply equally well to any of the other radial positions in the mesh. In this, the 1D spectrum is determined by averaging based on a finite Fourier transform of the individual streamwise lines of data points in the grid. Included in the figure are fitted lines obeying a $k^{-5/3}$ power law that are determined by averaging over the region where $E(k)k^{5/3}$ is approximately constant. Small parallel shifts to the fitted lines have no effect on the subsequent discussion other than small, immaterial, quantitative changes to the computed quantities.

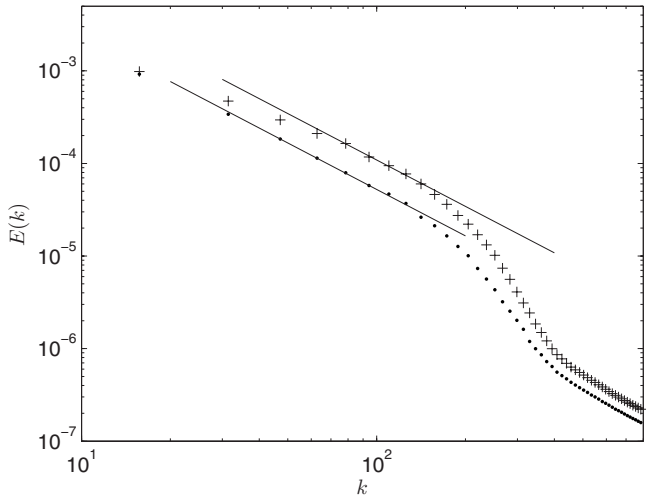

FIG. 24. 1D energy spectrum at $r=0.32$: +, $U_c=1/5$, $x=6.25$; ·, $U_c=1/3$, $x=8.25$. Straight lines are $\sim k^{-5/3}$.

The values of ϵ determined by this technique as a function of radial position for the two simulations are shown in Fig. 25, where they are seen to be essentially constant across the core region of the jet. Also shown in Fig. 25 are estimates of the rms streamwise velocity variance u' and Taylor microscale λ determined from the same data sets. The latter is computed by fitting a parabola at $s=0$ to the calculated two-point longitudinal correlation function $R_{11}(\mathbf{x},s) \equiv \overline{u(\mathbf{x})u(\mathbf{x}+s\mathbf{e}_1)}/\overline{u^2}(\mathbf{x})$. As in the case of ϵ, the values of λ and u' are also nearly constant along the central part of the jet.

Between the two cases considered here, the 1/3 coflow has a smaller velocity variance, a larger λ, and a significantly smaller dissipation rate. Besides the somewhat obvious effect of coflow in producing different levels of shearing, the differences in Fig. 25 reflect the influence that numerical parameters, such as tube length, have on establishing the smallest resolved scales in the simulation. Numerical parameters

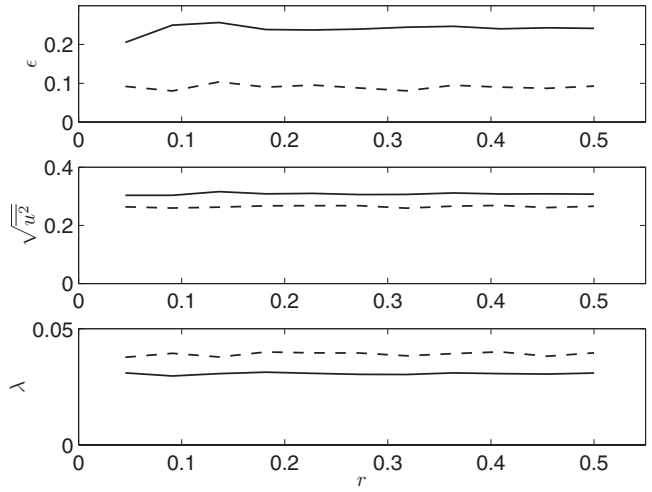

FIG. 25. Computed distribution of ϵ, $\sqrt{\overline{u^2}}$, and λ: –, $U_c=1/5$, $x=6.25$; - - -, $U_c=1/3$, $x=8.25$.

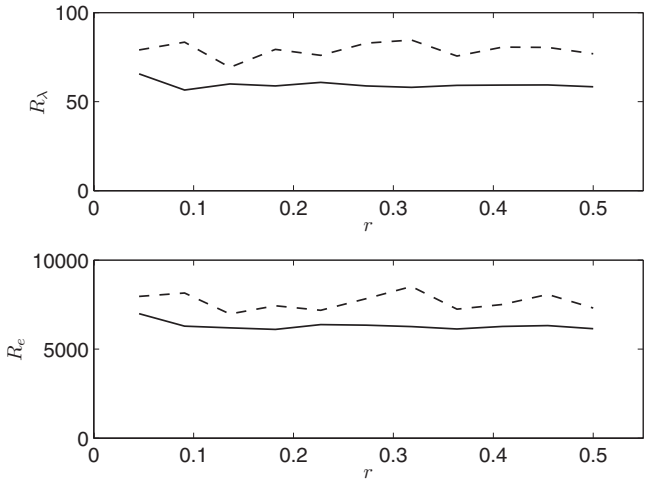

FIG. 26. R_λ and R_e across the jet core region: —, $U_c=1/5$, $x=6.25$; - - -, $U_c=1/3$, $x=8.25$.

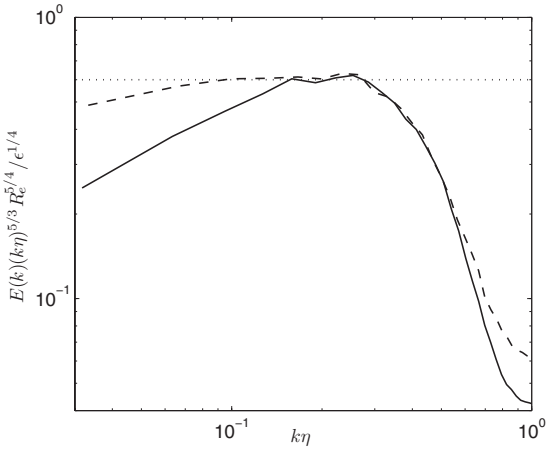

FIG. 27. Compensated energy spectrum in Kolmogorov variables: —, $U_c=1/5$, $x=6.25$; - - -, $U_c=1/3$, $x=8.25$. Dotted horizontal line represents $C_K=0.60$.

must affect how the 1D energy spectrum and the two-point correlation functions are realized, a connection that has yet to be established more fully. As one example of the subtleties involved, it may be noted that λ is smaller than h for the 1/5 coflow simulation yet larger than h in the case of the 1/3 coflow.

Figure 26 displays the results of using the quantities whose values are shown in Fig. 25 to arrive at a determination of R_e and R_λ. Consistent with the absence of significant variation in the constituent fields, the local and global Reynolds numbers are essentially unchanging over the jet core. Of course, one must expect that R_e, which may be interpreted as the inverse of the viscosity, is constant everywhere in the flow domain. An average of the Reynolds number values in the figure suggests that the 1/5 coflow jet at $x=6.25$ is characterized by $R_\lambda \approx 60$ and $R_e \approx 6312$ while the 1/3 coflow jet at $x=8.25$ has $R_\lambda \approx 79$ and $R_e \approx 7653$. These are relatively modest values that imply that loop removal is quite effective in replacing what would nominally be a model of inviscid Euler flow, with a model of turbulent flow at finite viscosity. That the higher Reynolds number is associated with the smaller tubes is to be expected since the degree to which the small scales are resolved is the primary distinguishing feature between any two simulations that have been scaled similarly in terms of U_{CL} and D.

With the Reynolds number known it is straightforward to evaluate the Kolmogorov length and time scales given, respectively, by

$$\eta = \frac{1}{R_e^{3/4}\epsilon^{1/4}} \tag{14}$$

and

$$\tau = \frac{1}{(\epsilon R_e)^{1/2}}. \tag{15}$$

These have average values across the jet core given by $\eta=0.0020$ and $\tau=0.026$ for the 1/5 coflow and $\eta=0.0022$ and $\tau=0.038$ for the 1/3 coflow. The values of η are significantly smaller than the respective λ values as well as the spatial resolution implied by the length of the vortex tubes. τ falls in the range of the time step $\Delta t=0.04$ used in marching the simulations forward in time. In a general sense the computed values of the scales are consistent with viewing the vortex simulation with loop removal as a LES with dissipation scales lying in the subgrid.

A plot of the compensated spectrum in which $E(k)$ is multiplied by $k^{5/3}$ and normalized by Kolmogorov variables is given in Fig. 27 for the same cases shown in Fig. 24. Consistent with the choice of $C_K=0.60$, the compensated spectrum is approximately constant at this value. Moreover, the extent of the constant region is greater for the simulation with the larger of the two Reynolds numbers. A subtle aspect of the figure, which also occurs at most of the r positions where the spectrum is computed, is the presence of a small bump or plateau in the curve just to the right of the flat, inertial range region. Such a feature has been seen in a number of DNS simulations of homogeneous isotropic turbulence.[36–38] Finally, it can be construed from the figure that the inertial range in the simulation is roughly in the interval $0.1 \leq k\eta \leq 0.2$ for the 1/3 coflow, which is a slightly higher range than in DNS of isotropic turbulence[36] for which the upper end is at 0.05.

For the inertial range scales, the structure function $S_2(s)=[u(\mathbf{x}+s\mathbf{e}_1)-u(\mathbf{x})]^2$ is expected to have $s^{2/3}$ power law behavior given by

$$S_2(s) = C_S(s\epsilon)^{2/3}, \tag{16}$$

with C_S a constant. In fact, Eq. (16) provides an alternative means of estimating dissipation rate and consequently Reynolds number. Thus, equating an empirical fit, say, $C_2 s^{2/3}$, to Eq. (16) gives the estimate

$$\epsilon = (C_2/C_S)^{3/2}. \tag{17}$$

The Reynolds numbers that have been discerned for the simulations may be regarded as not being high enough for the flow to have a fully isotropic inertial range. In this case, according to DNS simulations,[36] C_S is likely to be substantially smaller than its isotropic value, $C_S=4.02$ $C_K=2.13$. In fact, the compatibility of the 1D energy spectra shown in Fig.

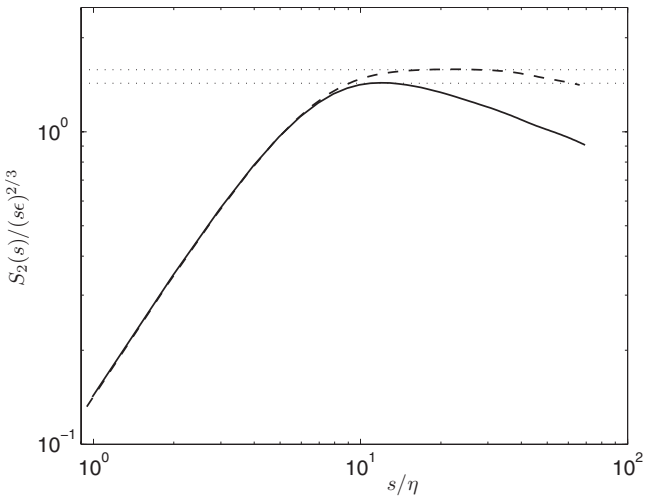

FIG. 28. Compensated structure function: —, $U_c=1/5$, $x=6.25$; - - -, $U_c=1/3$, $x=8.25$. Dotted lines correspond to $C_S=1.43$ and 1.58, respectively, for the two cases.

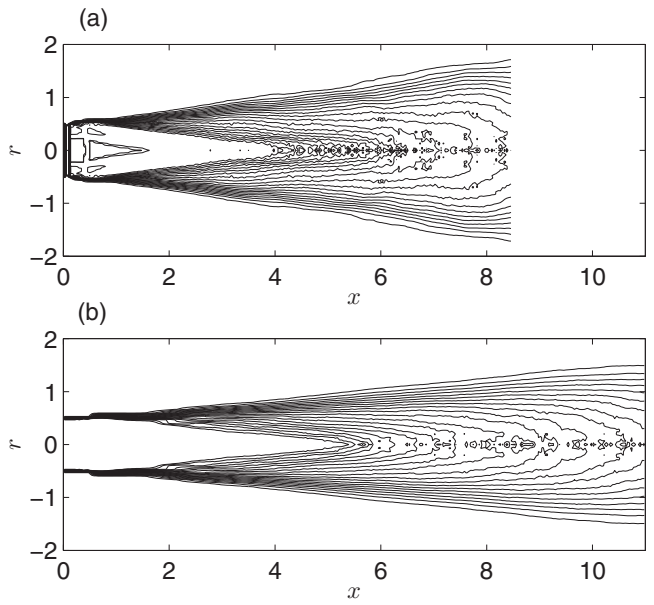

FIG. 29. Axisymmetric mean contours of the scalar concentration. (a) $U_c=1/5$; (b) $U_c=1/3$.

27 with the structure functions computed from the same data sets can be tested by evaluating C_S from Eq. (17) for given ϵ and C_2 and seeing how these compare to values at similar R_λ studied in DNS.[36] After determining C_2 from the raw data for $S_2(s)$, the plot of compensated structure functions $S_2(s)\times(s\epsilon)^{-2/3}$ shown in Fig. 28 may be made. The horizontal lines in the plot correspond to the particular value of $C_S=1.43$ for the 1/5 coflow at $R_\lambda=60$ and $C_S=1.58$ for the 1/3 coflow at $R_\lambda=79$. The appearance of these results has considerable qualitative agreement with the shear-free isotropic flow,[36] including the relative change between the two curves, though the numerical values are displaced lower by approximately 0.24. Such discrepancies can be accounted for by the many factors affecting the estimates, such as the sensitivity to the ϵ prediction. On the whole, it appears that the simulated turbulence in the round jet can be said to have physical characteristics similar to those in other numerical simulations in a similar Reynolds number range.

VIII. SCALAR FIELD

By adding passive tracer particles to the simulated jets, the discussion can be broadened to include the mixing of a contaminant laden jet with the environment. Either discrete particles or concentration fields deduced from particle densities in fixed volumes can be considered. In the latter case, turbulent diffusion of the scalar field is assumed to be sufficiently dominant so that it is not necessary to include an appropriate random walk to model molecular diffusion at a finite Schmidt number. The results computed here are compared to concentration fields determined in the experiments of Chu *et al.*[27]

Particles are seeded into the developing jet at the orifice from a unit disk of points similar in appearance to that shown in Fig. 23. Thus, each tracer may be viewed as being at the center of a small volume of fluid $V_t=\pi\Delta t/(4N_t)$ that enters the domain at each time step. Here, N_t is the number of particles covering the inlet. Since the incoming fluid has unit concentration, each tracer is assigned mass $m=V_t$. The concentration at subsequent times at the ith collection volume V_i is estimated to be $c_i=N_iV_t/V_i$ where N_i is the number of particles in V_i at a given time. The scalar field is computed for the case of the 1/5 and 1/3 coflows. These have coarse ($N_t=225$) and extremely fine ($N_t=5041$) representations in terms of tracers, respectively. The latter allows for smoother instantaneous predictions of concentration field, though, with suitable time averaging, the mean statistics appear to be equally well accounted for in both cases.

A view of the axisymmetric concentration field for the two coflows is shown in Fig. 29. At $U_c=1/3$, the average includes 400 consecutive records covering an elapsed time of 16, while for the 1/5 coflow 27 fields are averaged covering a time interval of 5.4. While further averaging might be desirable, the figure makes clear the influence of the greater shear in the 1/5 coflow case in increasing the spreading rate of the scalar, besides the reduced length of the core region. The pure conical shape of the core region in both cases is apparent as well and has the same appearance as in experiments.[10]

The maximum mean concentration field, located on the centerline at every position forms the basis of the normalized centerline dilution[27] defined as $1/[\Lambda\bar{C}(x,0)]$. Here and henceforth, to compensate for the reduced averaging at the jet center, the centerline mean scalar is taken to be an appropriate weighted average of the mean scalar in the small region $r\leq 0.167$ surrounding the central axis. Comparison of the centerline dilution with data from a variety of experiments as described by Chu *et al.*[27] is given in Fig. 30. Similar to the results for the velocity excess in Fig. 11, the dilution of the scalar field with downstream distance is seen to fall within a range that is consistent with the measured values.

Similar to Figs. 6 and 7, Fig. 31 compares measured and computed distributions of the normalized mean scalar field $\bar{C}(x,r)/\bar{C}(x,0)$ across the jet width. The radial distance is

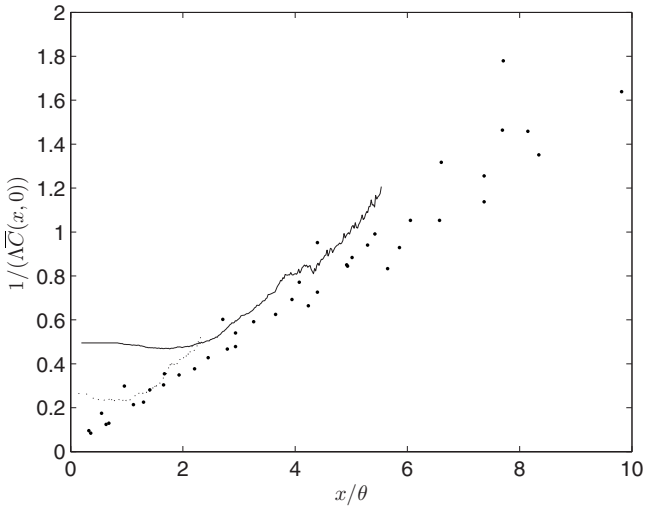

FIG. 30. Normalized centerline dilution for the concentration field. ●, physical experiments (Ref. 27). Simulations: —, $U_c=1/3$; ⋯, $U_c=1/5$.

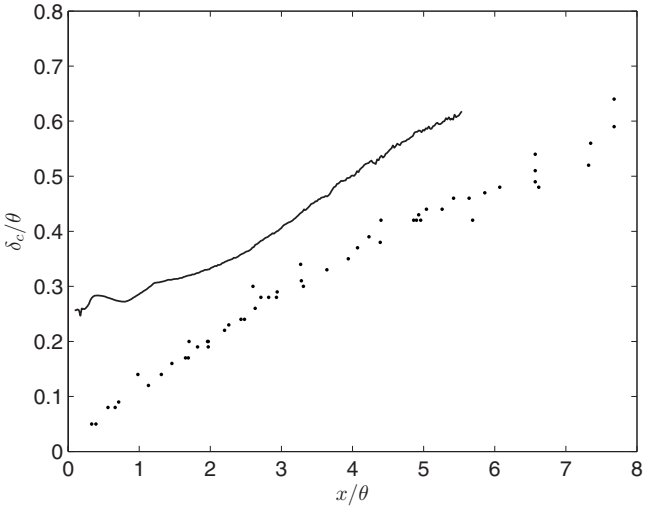

FIG. 32. Scalar half width. ●, physical experiments (Ref. 27); —, simulation with $U_c=1/3$.

scaled in terms of the concentration width δ_c, defined by the condition that $\overline{C}(x,\delta_c)/\overline{C}(x,0)=1/e$. The computed curve, which is typical of those in both of the scalar jet calculations, shows behavior that is somewhat off from a Gaussian. In particular, the lateral spread of the calculated concentration is somewhat less than that in the experiments while the distribution near the centerline compensates by being fuller than the Gaussian. From this figure it appears that the computed field is in a middle stage of transitioning from a top hat profile at the inlet to what may very well become Gaussian further downstream. While the experimental data here are at substantially higher Λ values, in fact, close to 10, compared to the simulation having $\Lambda=2$, perhaps a more important difference is that the experiments are at many more orifice diameters downstream, thus providing greater distance for Gaussianity to develop. This behavior is distinctly different than the case of the mean velocity field that reaches Gaussianity well within the extent of the current simulations as seen previously.

As for the concentration width, Fig. 32 shows a plot of the streamwise growth in δ_c compared to experiment[27] where it seen to have a similar growth rate but significantly greater magnitude. To some extent this reflects the non-Gaussianity of the simulated field which has yet to achieve a form independent of the inlet distribution. The contrast between this behavior and that of the mean velocity field is highlighted in Fig. 33 comparing the mean concentration and velocity profiles at the identical position $x=8.75$ in the 1/3 coflow jet. These curves show that velocity and concentration have the same extent of penetration into the ambient, coflowing fluid, a fact that is evident from instantaneous visualizations of the tracer particles and velocity contours. The significant difference between the mean fields is in the more uniform spread of the concentration field over the jet than the velocity field.

It has been often noted[6] that the scalar concentration tends to be relatively well mixed over individual large eddies that comprise the principal structure of the transitional and early turbulent jet. This implies that only sufficiently far downstream as the eddies break up into a finer scale turbulent structure can a Gaussian distribution of mean scalar

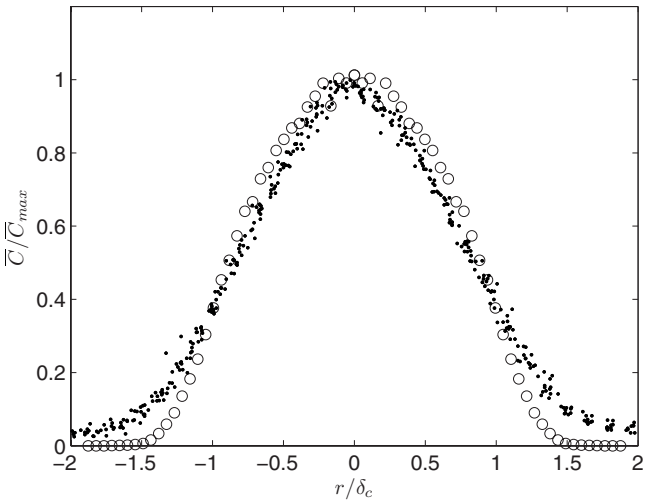

FIG. 31. Normalized concentration across the jet. ●, physical experiments (Ref. 27); ○, simulation with $U_c=1/3$, $x=10.86$.

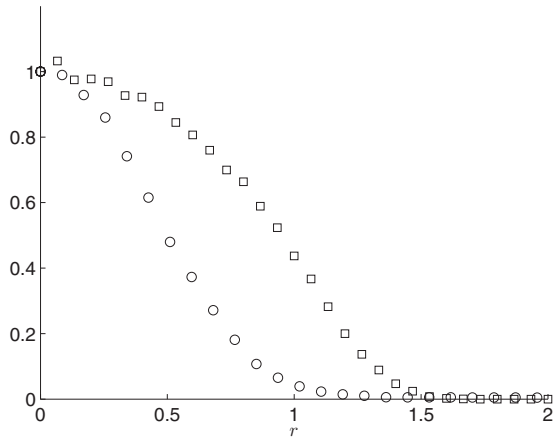

FIG. 33. Normalized mean velocity and concentration across the 1/3 coflow jet at $x=8.75$: ○, velocity; □, concentration.

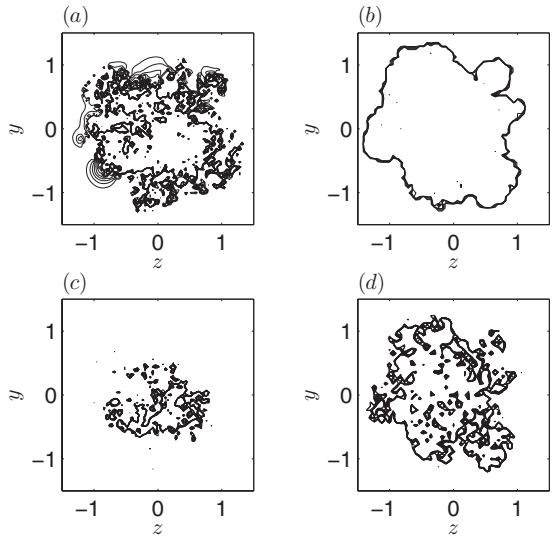

FIG. 34. End-on contours at $x=8.75$ in the 1/3 co-flow jet: (a) $0.025 \le (U-U_c)/(1-U_c) \le 0.25$; (b) $0.025 \le C \le 0.25$; (c) $0.75 \le (U-U_c)/(1-U_c) \le 1$; (d) $0.75 \le C \le 1$.

emerge. In contrast, the velocity field is determined everywhere as a summation over a distribution of turbulent vortices of varying strengths and orientations that evidently promotes the early onset of Gaussianity.

These points are supported by Fig. 34 showing end-on contour plots at $x=8.75$ in the 1/3 coflow jet of the velocity and concentration fields. Images (a) and (c) to the left are of the instantaneous normalized velocity, while (b) and (d) are of the concentration field. The top images, (a) and (b), contrast contours between 0.025 and 0.25 spaced at intervals of 0.025, while the lower two figures, (c) and (d), contain contours between 0.75 and 1, also at intervals of 0.025. Considering (a) and (b) at the smaller contour values, there is a dramatic difference between the concentration field—that is confined to the edge of the domain of tracer particles—and the far more dispersed velocity field. A different situation occurs with images (c) and (d) in Fig. 34 for the upper range of contour levels. Here, the largest scalar contours are distributed over most of the cross section of the jet, while those of the velocity are confined to the center. It was noted previously in reference to Fig. 15 that the turbulence regime prior to the downstream boundary contains many large eddies whose provenance is in the more organized upstream structures. Evidently, the further downstream dissolution of these into smaller scale eddies—within each of which the scalar contaminant is presumably well mixed—is a requirement for the emergence of complete Gaussianity in the jet scalar field.

IX. CONCLUSIONS

This paper has considered the simulation of the turbulent coflowing jet via a grid-free vortex filament scheme incorporating loop removal as a de facto subgrid model. The coflowing jet flows produced by the method were seen to have length scales and velocity statistics that fit in well with a number of physical experiments. The vortical make up of the transition was fully consistent with experiments including a major role for the development and growth of streamwise vorticity. The special relationship of the latter to the lateral spread of the jet through entrainment and the ejection of fluid from the jet core was observed in detail. Through the use of tracer particles the range of the study was expanded to include analysis of the spread of a scalar jet into an ambient coflowing fluid. The rapid appearance of Gaussianity in the mean velocity distribution was not matched by the mean concentration field. The contrasting behaviors appear to reflect different underlying mechanisms in their dispersion, with the concentration field depending on the complete dissolution of large eddies within which the scalar field is well mixed.

A significant interest of this work, motivated in part by the relatively new status of the vortex filament approach as a LES scheme, was in exploring some of the dependencies of the method on numerical parameters. A major part of this was in establishing a connection between the Reynolds number and the use of loop removal with its implied dissipation rate. For the Reynolds number range corresponding to the simulations, the jet turbulence was observed to have statistical properties agreeing well with established results for turbulence determined from DNS.

Finally, it may be concluded that the vortex filament scheme achieves one of the primary goals of LES, namely, to capture essential large scale features of the turbulence without the necessity of resolving small viscous scales or carefully selecting a specific subgrid model and its parameters. For the coflowing jet this was particularly evident in the capability of the scheme in reproducing subtle aspects of the physics such as the effect of coflow on the length of the potential core. This encourages future studies that will utilize the approach in modeling particle dispersion, sound generation, and other complex phenomena that depend on a robust treatment of the underlying turbulent eddies. Future plans also include advances in expanding the numerical efficiency so that an order of magnitude increase in the number of vortex elements is feasible. This will enable an expansion of the jet simulations to encompass the entire spatial development from the orifice through transition to the self-similar far field.

ACKNOWLEDGMENTS

The author would like to thank Professor Joseph Hun-Wei Lee and Professor Mark Davidson for supplying experimental data used in the comparisons. The assistance of Dr. P. Collins and Dr. M. Potts in the development and use of the Vorcat, Inc. implementation of the 3D vortex filament method is appreciated. This research was supported in part by the National Science Foundation through TeraGrid resources provided by the Pittsburgh and San Diego Supercomputing Centers.

[1] J. Hileman and M. Samimy, "Turbulence structures and the acoustic far field of a Mach 1.3 jet," AIAA J. **39**, 1716 (2001).
[2] J. R. Debonis and J. N. Scott, "Large-eddy simulation of a turbulent compressible round jet," AIAA J. **40**, 1346 (2002).
[3] C. Bogey and C. Bailly, "Investigation of downstream and sideline subsonic jet noise using large eddy simulation," Theor. Comput. Fluid Dyn. **20**, 23 (2006).

[4]J. N. Chung and T. R. Troutt, "Simulation of particle dispersion in an axisymmetric jet," J. Fluid Mech. **186**, 199 (1988).
[5]E. K. Longmire and J. K. Eaton, "Structure of a particle-laden round jet," J. Fluid Mech. **236**, 217 (1992).
[6]T. P. Jenkins and I. M. Kennedy, "Measurements of aerosol product in an axisymmetric co-flow jet," Exp. Fluids **29**, 532 (2000).
[7]M. Olsson and L. Fuchs, "Large eddy simulation of the proximal region of a spatially developing circular jet," Phys. Fluids **8**, 2125 (1996).
[8]A. T. Webb and N. N. Mansour, "Toward LES models of jet and plumes," Center for Turbulence Research, Annual Research Briefs, 2000, pp. 229–240.
[9]W. Zhao, S. H. Frankel, and L. Mongeau, "Large eddy simulations of sound radiation from subsonic turbulent jets," AIAA J. **39**, 1469 (2001).
[10]A. Borg, J. Bolinder, and L. Fuchs, "Simultaneous velocity and concentration measurements in the near field of a turbulent low-pressure jet by digital particle image velocimetry-planar laser-induced fluorescence," Exp. Fluids **31**, 140 (2001).
[11]C. Bogey and C. Bailly, "Large eddy simulations of round free jets using explicit filtering with/without dynamic Smagorinsky model," Int. J. Heat Fluid Flow **27**, 603 (2006).
[12]E. G. Puckett, in *Incompressible Computational Fluid Dynamics: Trends and Advances*, edited by M. D. Gunzburger and R. A. Nicolaides (Cambridge University Press, Cambridge, 1993), pp. 335–407.
[13]J. C. Agui and L. Hesselink, "Flow visualization and numerical analysis of a coflowing jet: A three-dimensional approach," J. Fluid Mech. **191**, 19 (1988).
[14]J. E. Martin and E. Meiburg, "Numerical investigation of three-dimensionally evolving jets subject to axisymmetric and azimuthal perturbation," J. Fluid Mech. **230**, 271 (1991).
[15]J. E. Martin and E. Meiburg, "Numerical investigation of three-dimensionally evolving jets under helical perturbations," J. Fluid Mech. **243**, 457 (1992).
[16]Y. M. Marzouk and A. F. Ghoniem, "Vorticity structure and evolution in a transverse jet," J. Fluid Mech. **575**, 267 (2007).
[17]R. Yokota, T. K. Sheel, and S. Obi, "Calculation of isotropic turbulence using a pure Lagrangian vortex method," J. Comput. Phys. **226**, 1589 (2007).
[18]G.-H. Cottet, B. Michaux, S. Ossia, and G. VanderLinden, "A comparison of spectral and vortex methods in three-dimensional incompressible flows," J. Comput. Phys. **175**, 702 (2002).
[19]P. Chatelain, A. Chrioni, M. Bergdorf, D. Rossinelli, W. Andreoni, and P. Koumoutsakos, "Billion vortex particle direct numerical simulations of aircraft wakes," Comput. Methods Appl. Mech. Eng. **197**, 1296 (2008).
[20]G. Winckelmans, R. Cocle, L. Dufresne, and R. Capart, "Vortex methods and their applications to trailing wake vortex simulations," C. R. Phys. **6**, 467 (2005).
[21]A. J. Chorin, "Hairpin removal in vortex interactions. II.," J. Comput. Phys. **107**, 1 (1993).
[22]A. J. Chorin, *Vorticity and Turbulence* (Springer, New York, 1994).
[23]P. S. Bernard, "Turbulent flow properties of large scale vortex systems," Proc. Natl. Acad. Sci. U.S.A. **103**, 10174 (2006).
[24]P. S. Bernard, "Grid-free simulation of the spatially growing turbulent mixing layer," AIAA J. **46**, 1725 (2008).
[25]L. Greengard and V. Rohklin, "A fast algorithm for particle simulations," J. Comput. Phys. **73**, 325 (1987).
[26]D. Liepmann and M. Gharib, "The role of streamwise vorticity in the near-field entrainment of round jets," J. Fluid Mech. **245**, 643 (1992).
[27]P. Chu, J. Lee, and V. Chu, "Spreading of turbulent round jet in coflow," J. Hydraul. Eng. **125**, 193 (1999).
[28]T. B. Nickels and A. E. Perry, "An experimental and theoretical study of the turbulent coflowing jet," J. Fluid Mech. **309**, 157 (1996).
[29]M. J. Davidson and H. J. Wang, "A strongly-advected jet in a coflow," J. Hydraul. Eng. **128**, 742 (2002).
[30]B. J. Boersma, G. Brethouwer, and F. T. M. Nieuwstadt, "A numerical investigation on the effect of the inflow conditions on the self-similar region of a round jet," Phys. Fluids **10**, 899 (1998).
[31]R. A. Antonia and R. W. Bilger, "An experimental investigation of an axisymmetric jet in a co-flowing air stream," J. Fluid Mech. **61**, 805 (1973).
[32]S. C. Crow and F. H. Champagne, "Orderly structure in jet turbulence," J. Fluid Mech. **48**, 547 (1971).
[33]T. R. Meyer and J. C. Dutton, "Experimental study of the mixing transition in a gaseous axisymmetric jet," Phys. Fluids **13**, 3411 (2001).
[34]J. Westerweel, T. Hofmann, C. Fukushima, and J. C. R. Hunt, "The turbulent/non-turbulent interface at the outer boundary of a self-similar turbulent jet," Exp. Fluids **33**, 873 (2002).
[35]K. R. Sreenivasan, "On the universality of the Kolmogorov constant," Phys. Fluids **7**, 2778 (1995).
[36]P. K. Yeung and Y. Zhou, "Universality of the Kolmogorov constant in numerical simulations of turbulence," Phys. Rev. E **56**, 1746 (1997).
[37]T. Gotoh, D. Fukayama, and T. Nakano, "Velocity field statistics in homogeneous steady turbulence obtained using a high-resolution direct numerical simulation," Phys. Fluids **14**, 1065 (2002).
[38]Y. Kaneda, T. Ishihara, M. Yokohawa, K. Itakura, and A. Uno, "Energy dissipation rate and energy spectrum in high resolution direct numerical simulations of turbulence in a periodic box," Phys. Fluids **15**, L21 (2003).